Structural organization and dynamics of FCHo2 docking on membranes

F. El Alaoui[1], I. Casuso[2], D. Sanchez-Fuentes[3], C. André-Arpin[1], R. Rathar[3], V. Baecker[4], A. Castro[5], T. Lorca[5], J. Viaud[6], S. Vassilopoulos[7], A. Carretero-Genevrier[3], L. Picas[1,*].

[1]Institut de Recherche en Infectiologie de Montpellier (IRIM). CNRS UMR 9004 – Université de Montpellier, Montpellier, France.

[2]U1067 INSERM, Aix-Marseille Université, Marseille, France

[3]Institut d'Électronique et des Systèmes (IES), CNRS UMR 5214 – Université de Montpellier, Montpellier, France.

[4]Montpellier Ressources Imagerie, BioCampus Montpellier, CNRS, INSERM, University of Montpellier, 34000 Montpellier, France.

[5]Centre de Biologie Cellulaire de Montpellier (CRBM). CNRS UMR – Université de Montpellier, Montpellier, France.

[6]Institute of Metabolic and Cardiovascular Diseases (I2MC), UMR1297, Toulouse, France; University of Toulouse, Paul Sabatier University, Toulouse, France.

[7]Sorbonne Université, INSERM, Institute of Myology, Centre of Research in Myology, UMRS 974, Paris, France.

[*]Correspondence sent to: laura.picas@irim.cnrs.fr

Abstract

Clathrin-mediated endocytosis (CME) is a central trafficking pathway in eukaryotic cells regulated by phosphoinositides. The plasma membrane phosphatidylinositol-4,5-bisphosphate ($PI(4,5)P_2$) plays an instrumental role in driving CME initiation. The F-BAR domain only protein 1 and 2 complex (FCHo1/2) is among the early proteins that reach the plasma membrane, but the exact mechanisms triggering its recruitment remain elusive. Here, we show the molecular dynamics of FCHo2 self-assembly on membranes by combining minimal reconstituted *in vitro* and cellular systems. Our results indicate that $PI(4,5)P_2$ domains assist FCHo2 docking at specific membrane regions, where it self-assembles into ring-like shape protein patches. We show that the binding of FCHo2 on cellular membranes promotes $PI(4,5)P_2$ clustering at the boundary of cargo receptors and that this accumulation enhances clathrin assembly. Thus, our results provide a mechanistic framework that could explain the recruitment of early $PI(4,5)P_2$-interacting proteins at endocytic sites.

Introduction

The biogenesis of clathrin-coated vesicles requires precise and coordinated recruitment of more than ~ 50 different proteins to undergo the bending, elongation, and fission of the plasma membrane(1, 2). Different factors assist in recruiting endocytic proteins, such as the interaction with phosphoinositides(3), curvature sensing, and protein-protein interactions(4). Also, the resistance of the plasma membrane that results from membrane-cytoskeleton adhesion sets the rate of forming transport vesicles(5). Although the initiation of endocytosis is a critical step, the exact mechanism triggering the nucleation of endocytic proteins at the plasma membrane is not well understood. The early stages of CME entail the nucleation of adaptor and accessory proteins, cargo, and lipids to undergo the bending of the plasma membrane(6). Several studies have shown that FCHo1/2 (Fer/CIP4 homology domain only protein 1 or 2) is among the early proteins recruited at endocytic sites(1, 7), where it establishes a network of interactions with pioneer proteins, such as Eps15, adaptor protein 2 (AP2), and transmembrane cargo(1, 8, 9). FCHo paralogs associate with membranes through the dimerization of F-BAR domains displaying a shallow concave surface that interacts with acidic phospholipids(7, 10, 11). A polybasic motif follows the F-BAR scaffold and provides a selective recognition for $PI(4,5)P_2$(8). Finally, FCHo1/2 is flanked at the C-terminal by a μ-homology domain (μ-HD) that directly binds with multiple early endocytic proteins such as Eps15, intersectin 1 or CALM(7, 8, 12). Indeed, FCHo1/2 is required to recruit Eps15 on membranes(13), and the assembly of a FCHo1/2-Eps15-AP2 complex is essential to drive efficient cargo loading(8). The recruitment of FCHo1/2 on membranes is central to initiate the endocytic activity but, the underlying molecular mechanism remains unclear.

Here we combined sub-diffraction microscopy and high-speed atomic force microscopy (HS-AFM) with *in vitro* and *in cellulo* reconstituted systems to show that $PI(4,5)P_2$ domains regulate FCHo2 docking on flat membranes, where it self-assembles into ring-like shaped protein structures that are compatible with the size and temporal scale of clathrin-mediated endocytosis. Our results indicate that, in the absence of metabolizing enzymes, FCHo2 can engage a local $PI(4,5)P_2$ enrichment at the boundaries of clathrin-regulated cargo receptors and enhance the formation of clathrin-positive assemblies. Finally, manipulation of membrane curvature through lithographic approaches showed that $PI(4,5)P_2$ promotes the partition of FCHo2 at the edges of dome-like structures. Collectively, our work points out $PI(4,5)P_2$ lateral lipid heterogeneities as an organizing mechanism supporting the docking and self-organization of $PI(4,5)P_2$-interacting proteins that, like FCHo2, participate in the initial stages of CME.

Results

FCHo1/2 drives PI(4,5)P_2 clustering formation on cellular membranes

To study FCHo1/2 recruitment on cellular membranes, we monitored by airyscan microscopy the binding of recombinant full-length FCHo2-Alexa647 on plasma membrane sheets. We generated plasma membrane sheets by ultrasound-mediated unroofing of cells stably expressing the transferrin receptor (TfR-GFP) as a model of cargo receptor regulated by FCHo1/2(7). We monitored the subcellular dynamics of lipids using TopFluor fatty acid conjugates, as previously reported(14). Thus, we loaded HT1080 unroofed cells with fluorescent PI(4,5)P_2 (TF-TMR-PI(4,5)P_2) or phosphatidylserine as a control (PS, TF-TMR-PS) (Figure 1A and B). We characterized the steady-state organization of fluorescent PI(4,5)P_2 and its ability to form domains as compared to other anionic lipids (Figure 1-figure supplement 1), in agreement with previous numerical simulations(15). The functionality of recombinant FCHo2 was determined by performing a tubulation assay using membrane sheets made of brain polar lipids, as previously reported(16) (Figure 1-figure supplement 2). Kymograph analysis on plasma membrane sheets showed that FCHo2 is preferentially recruited to PI(4,5)P_2-enriched domains often co-localized with the TfR (Figure 1-figure supplement 3). We found that the kinetics of FCHo2 recruitment on these regions was faster than in the absence of PI(4,5)P_2 enrichment. To determine that the spatial recruitment of FCHo2 is promoted by PI(4,5)P_2, we monitored the protein binding on supported lipid bilayers made of 20% of total negatively charged lipids and different % mol of PI(4,5)P_2. As expected, increasing amounts of PI(4,5)P_2 favored FCHo2 binding on flat membranes (Figure 1-figure supplement 4). The temporal analysis of FCHo2 recruitment also showed that binding to PI(4,5)P_2 domains resulted in the formation of long-lived FCHo2 puncta (Figure 1-figure supplement 5), whereas its association with a homogenous distribution of PI(4,5)P_2 was more likely to lead to FCHo2 disassembly. We observed that the F-BAR domain alone (i.e. without the region rich in positively charged amino acids of the extended F-BAR construct, F-BAR-x, described in(11)) also displayed preferential recruitment to PI(4,5)P_2 enriched regions, in agreement with the enhanced binding of the domain at 5 % mol of PI(4,5)P_2 (Figure 1-figure supplement 4). Collectively, these results confirm the functionality of full-length FCHo2-Alexa647 and indicate that PI(4,5)P_2-enriched regions facilitate FCHo2 docking on membranes.

The formation of PI(4,5)P_2 clusters at the plasma membrane orchestrates the recruitment of PI(4,5)P_2-binding proteins *via* ionic-lipid protein interactions(17, 18). Several structural domains of endocytic proteins, including the F-BAR domain of Syp1, locally accumulate PI(4,5)P_2 on *in vitro* membranes(19, 20), and we showed that BIN1 recruits its downstream partner dynamin through this mechanism. We thus investigated the impact of FCHo2 on PI(4,5)P_2 clustering formation. Injection of FCHo2-Alexa647 on TfR-GFP plasma membrane sheets led to the binding of FCHo2 and the formation of sub-micrometric puncta that co-localized with PI(4,5)P_2 and the TfR (Figure 1A).

Analysis of the protein dynamics showed that FCHo2 binding convoyed a redistribution of the $PI(4,5)P_2$ signal on TfR-GFP-positive puncta but not on PS labeled plasma membrane sheets (Figure 1B). To determine if FCHo2-mediated $PI(4,5)P_2$ enrichment was a general feature of FCHo2, we monitored its binding relative to another clathrin-regulated cargo, the EGF receptor (EGFR) (Figure 1C). In this case, we observed a concomitant increase of both the $PI(4,5)P_2$ and EGFR signal at FCHo2-positive puncta (Figure 1C and Figure 1-figure supplement 6), possibly as a result of the interaction of the EGFR juxtamembrane domain with $PI(4,5)P_2$(21). Quantification of the intensity of $PI(4,5)P_2$ domains in the absence of other endocytic proteins and ATP to prevent the activation of type I phosphatidylinositol 4-phosphate 5-kinase(22) confirmed a local increase in the $PI(4,5)P_2$ signal after the addition of FCHo2 on cellular membranes (Figure 1D). Therefore, pointing out that $PI(4,5)P_2$ clustering at the boundary of clathrin-regulated receptors is a direct effect of FCHo2 binding and not due to *de novo* production of $PI(4,5)P_2$.

To confirm that FCHo1/2 proteins induce $PI(4,5)P_2$ clustering formation *in cellulo*, we over-expressed FCHo1 and 2 in HT1080 cells. As previously reported, we confirmed that FCHo1/2 localized preferentially at the plasma membrane(7), organized into protein assemblies of different dimensions (Figure 1E). In agreement to what we observed on plasma membrane sheets, our *in cellulo* data showed a co-localization between FCHo1/2 and endogenous plasma membrane $PI(4,5)P_2$ (see methods section) (Figure 1E). Furthermore, we detected a significant increase in the average intensity of $PI(4,5)P_2$ domains in the presence of FCHo proteins (Figure 1F). Altogether, these results suggest that FCHo1/2 has the capability to accumulate $PI(4,5)P_2$ locally.

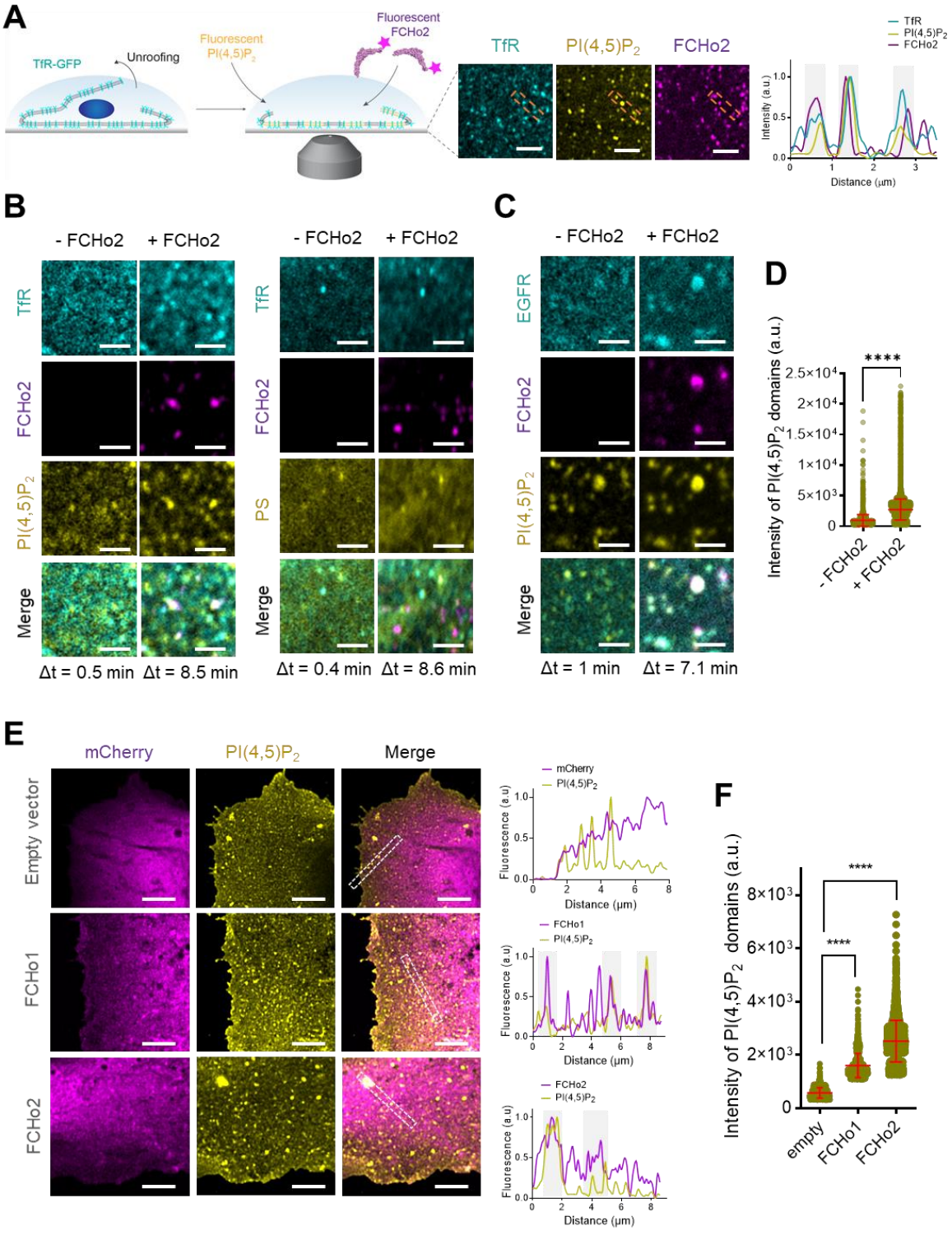

Figure 1. FCHo2 induces PI(4,5)P_2 clustering at the boundary of cargo receptors. (A) *Left*, cartoon of the experimental setup to monitor the recruitment of FCHo2-Alexa647 on cellular membranes loaded with fluorescent PI(4,5)P_2. *Right*, representative still airyscan images showing the co-localization of TfR-GFP (cyan), PI(4,5)P_2 (yellow) and FCHo2 (magenta) on plasma membrane sheets and cross-section analysis of FCHo2-positive puncta highlighted by the orange dashed box. Scale bar, 2 µm. (B, C) Representative z-projected time-lapse confocal images of plasma membrane sheets showing the co-localization of PI(4,5)P_2 or PS (yellow) and clathrin-regulated cargoes TfR or EGFR (cyan) before (- FCHo2) and after the addition of FCHo2 (+ FCHo2, magenta). The projected time interval (Δt) is specified below each image. Scale bar, 2 µm. (D)

Distribution of the intensity of PI(4,5)P_2 domains before (- FCHo2) and after addition of FCHo2 (+ FCHo2) on plasma membrane sheets. Mean ± s.d, in red. Welch's t-test (****, $P < 0.0001$). The number of PI(4,5)P_2 domains analyzed from three replicates was n=4397 and n=33815, respectively from at least three replicates. (E) Representative airyscan images showing a maximum intensity projection of one stack of the basal plasma membrane of HT1080 cells transiently transfected with either mCherry (empty vector), mCherry-FCHo1 or mCherry-FCHo2 (magenta) and stained for endogenous PI(4,5)P_2 (yellow). Cross-section analysis of plasma membrane regions highlighted by the white dashed box in the corresponding image. Scale bar, 4 µm. (F) Distribution of the intensity of PI(4,5)P_2 domains at the plasma membrane of cells transfected with either mCherry (empty), mCherry-FCHo1 (FCHo1) or mCherry-FCHo2 (FCHo2). Mean ± s.d, in red. One-way ANOVA (****, $P < 0.0001$). The number of PI(4,5)P_2 domains analyzed was n=1647, n=2164 and n=2608, respectively from three independent experiments.

Figure 1 – source data 1. Intensity of PI(4,5)P_2 domains.

FCHo2-mediated PI(4,5)P_2 clustering primes pre-endocytic events

We next analyzed if FCHo2-mediated PI(4,5)P_2 clustering participates in the formation of clathrin-coated structures. Both membrane activity and FCHo2 interaction with binding partners are required to direct clathrin-coated structures' growth and stability(23). Whereas the membrane-bending activity and interaction with negatively charged lipids is primarily encoded within the F-BAR domain(7), the interaction with AP2 and Eps15 is mediated by a downstream AP2-activating (APA) domain and C-terminal µ-HD(8, 9). We determined by immunofluorescence the formation of clathrin-positive puncta on supported lipid bilayers made of 20% of negatively charged lipids incubated with non-labeled F-BAR domain (residues 1 to 262), extended F-BAR domain (F-BAR-x, residues 1 to 430)(7), or full-length FCHo2 (Figure 2A-B). We reconstituted clathrin-coat assembly *in vitro* by using active cytosolic components from *Xenopus* egg extracts supplemented with ATP and GTPγS, as previously reported(24, 25). As expected, in the absence of FCHo2 the addition of cytosolic extracts leads to the appearance of clathrin-positive puncta, as compared to the ATP and GTPγS alone (Figure 2C and Figure 2-figure supplement 1). Under these conditions, we could also detect a residual signal of the FCHo2 antibody, corresponding to the endogenous protein present in the cytosolic extracts. Incubation of 1 µM of FCHo2 with cytosolic extracts on 5 % PI(4,5)P_2-containing lipid bilayers resulted in a 2-fold increase in the normalized intensity of the PI(4,5)P_2 signal on clathrin-positive puncta (Figure 2C and D), which is convoyed by a 7-fold increase in the normalized intensity of clathrin-positive spots (Figure 2C and E). We observed a moderate increase in the local intensity of both PI(4,5)P_2 and clathrin structures in the presence of the F-BAR domain alone, in agreement with its reported ability to assist PI(4,5)P_2 microdomain formation(19). Furthermore, this effect was intensified by the F-BAR-x, supporting the combined contribution of the APA domain(8, 23) and the enhanced tabulation effect of this construct(7) in promoting a local PI(4,5)P_2 enrichment and the formation of clathrin-positive structures (Figure 2 C-E). Replacement of PI(4,5)P_2 by PS preserved FCHo2 association with

membranes but prevented the detection of clathrin in our *in vitro* assay, supporting the functional role of PI(4,5)P_2 in clathrin-coat formation. Thus, these results indicate that, in addition to its membrane-remodeling activity, FCHo2 might promote clathrin assembly by clustering PI(4,5)P_2 and that the association with interacting partners in cytosolic extracts enhances this effect, possibly *via* the APA domain.

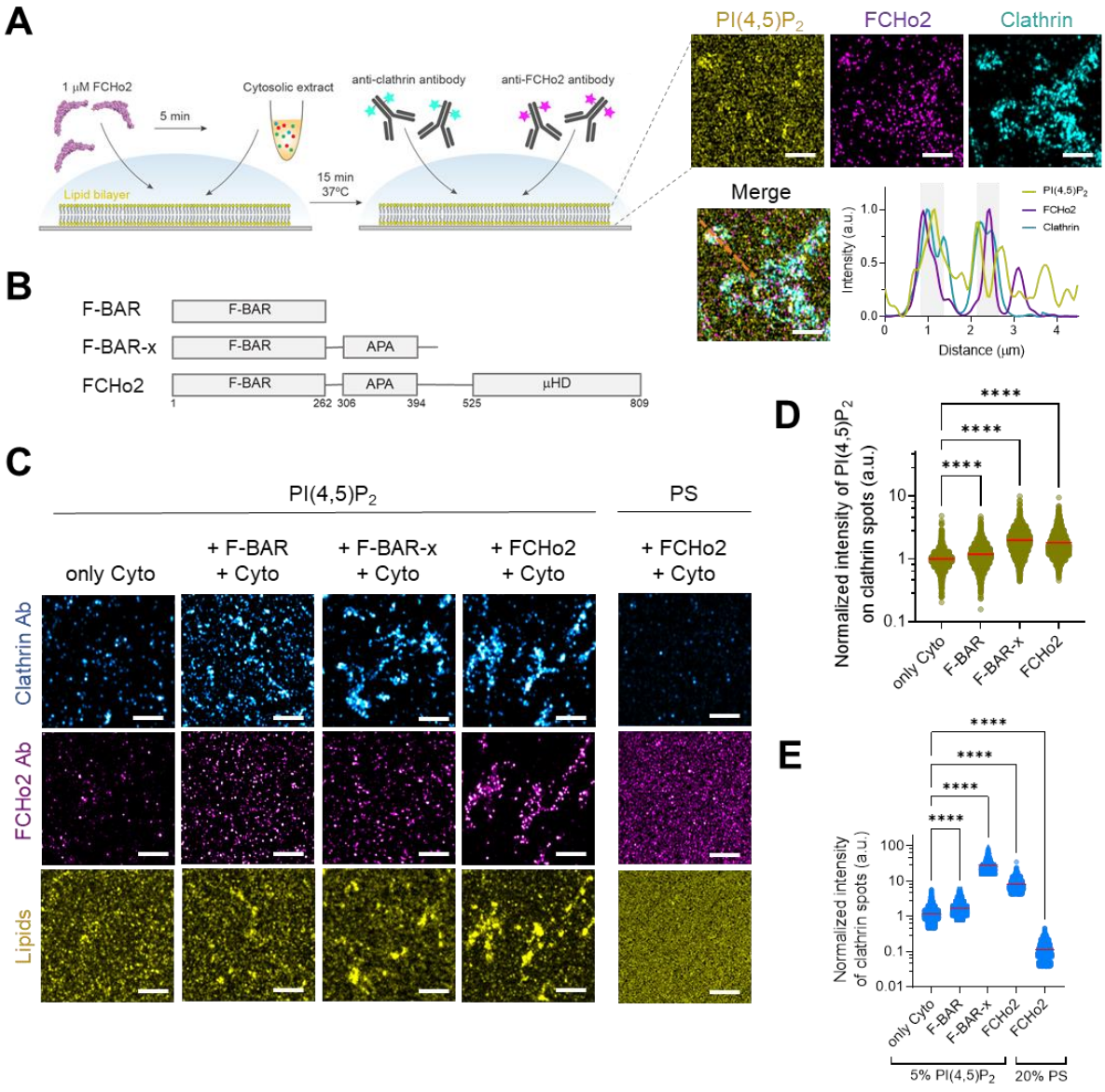

Figure 2. FCHo2 induces PI(4,5)P_2 clustering on clathrin-positive puncta. (A) *Left*, cartoon of the *in vitro* clathrin-coat assembly with cytosolic extracts and immunofluorescence assay to detect FCHo2 and clathrin-positive structures on 5% mol PI(4,5)P_2-containing supported lipid bilayers. *Left, r*epresentative still airyscan images on lipid bilayers doped with fluorescent PI(4,5)P_2 (yellow) showing the co-localization with FCHo2 (magenta) and clathrin (cyan). Intensity profile along the orange dotted line in the corresponding image. Scale bar, 2 µm. (B) Protein domain mapping of F-BAR domain (residues 1 to 262), F-BAR-x (residues 1 to 430), or full-length FCHo2 showing the F-BAR, APA and C-terminal µ-HD domains. (C) Representative airyscan images of lipid bilayers containing either 5% mol PI(4,5)P_2 or 20% PS (yellow) (total negative charge is 20%) that were incubated with recombinant FCHo2 (+ FCHo2), F-BAR domain (+ F-BAR) or F-BAR-x domain (+

F-BAR-x) and 4 mg/ml of cytosolic extracts (+ Cyto) or only with the cytosolic extract (only Cyto). Clathrin (blue) and FCHo2 (magenta) were detected by immunofluorescence (antibody, Ab). Scale bar, 2 µm. (D, E) Log10 scale distribution of the normalized intensity of fluorescent $PI(4,5)P_2$ on clathrin-positive structures and normalized intensity of clathrin structures, respectively, in the absence (only Cyto) or presence of either FCHo2, F-BAR or F-BAR-x combined to cytosolic extracts on $PI(4,5)P_2$ or PS-containing bilayers. Mean, in red. One-way ANOVA (****, $P < 0.0001$). The number of clathrin-positive spots analyzed was n=11564, n =9292, n=4719 n=2205, and n=1635, as set in the graph from at least three independent experiments.

Figure 2 – source data 1. Normalized intensity of $PI(4,5)P_2$ and intensity of clathrin spots.

Assembly of FCHo2 into molecular clusters prompts membrane bending

A characteristic hallmark of endocytic proteins on cellular membranes is their spatial organization into punctate structures(7, 8), and we systematically observed this feature on plasma membrane sheets and *in vitro* membranes (Figure 1 and Figure 1-figure supplement 5). Co-segregation of early endocytic proteins into sub-micrometer scale clusters relies on multivalent interactions(13). Therefore, we asked what might be the role of $PI(4,5)P_2$ in the spatial organization of FCHo2. We estimated by airyscan microscopy the average size of FCHo2 puncta on cellular membranes (i.e. plasma membrane sheets) and on 5% $PI(4,5)P_2$- containing bilayers after the addition of 1 µM of FCHo2-Alexa 647 (Figure 3A and B), which was on both cases ~ 0.067 μm^2. On lipid bilayers doped with 5% $PI(4,5)P_2$ we could also detect that the F-BAR domain alone can assemble into punctate structures, although the average size was ~ 0.094 μm^2. Interestingly, replacing 5% $PI(4,5)P_2$ by PS lead to a homogeneous surface distribution of FCHo2 and prevented the detection of sub-micrometric puncta. Therefore, suggesting that $PI(4,5)P_2$ multivalent interactions through the F-BAR promote FCHo2 segregation into molecular clusters.

Next, we used atomic force microscopy (AFM) to investigate FCHo2 molecular clusters at nanometer-scale resolution. Supported lipid bilayers doped with 5% $PI(4,5)P_2$ were formed on freshly cleaved mica disks (see methods section). Before adding proteins, we confirmed the homogeneity and absence of defects of supported bilayers under the imaging buffer. Injection of full-length FCHo2 at 1 µM in the imaging chamber resulted in sub-micrometric protein patches with a median dimension of ~ 0.005 μm^2 that protruded out of the flat membrane surface with an average height of ~ 47 ± 3 nm (Figure 3C-E). An increase in the setpoint force from minimal values (a few tens of pN) to intense forces (around one hundred pN) resulted in the reduction of the height of FCHo2 clusters down to ~ 15 ± 2 nm, thus suggesting that FCHo2 can moderately bend supported lipid membranes at minimal AFM imaging forces.

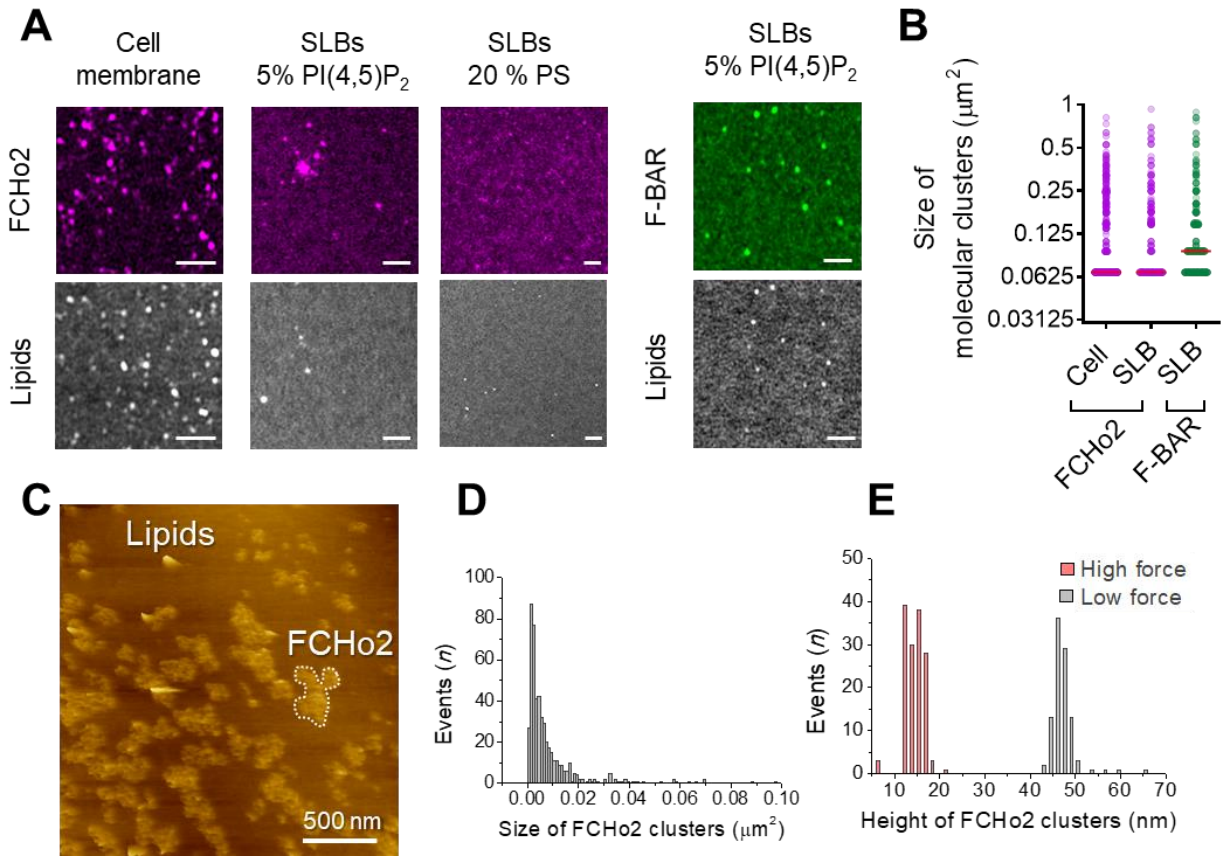

Figure 3. FCHo2 forms molecular clusters on PI(4,5)P_2-containing bilayers. (A) Representative airyscan images of plasma membrane sheets or lipid bilayers doped with either 5% mol PI(4,5)P_2 or 20% PS (total negative charge is 20%) and incubated with FCHo2-Alexa647 (magenta) or F-BAR-Alexa647 (green). Scale bar, 2 µm. (B) Size distribution of FCHo2 (magenta) and F-BAR (green) molecular clusters (in µm²) on plasma membrane sheets (cell) or lipid bilayers (SLB) containing 5 % mol of PI(4,5)P_2. Median value is displayed in red. The number of molecular clusters analyzed was n=10793, n=19287, and n=7028, as set in the graph from at least three independent experiments. (C) Representative AFM image of FCHo2 molecular clusters (white dashed region) on supported lipid bilayers containing 5% mol PI(4,5)P_2. (D) Size distribution of FCHo2 molecular clusters (in µm²) obtained from AFM images. (E) Height distribution of FCHo2 molecular clusters (in nm) at low (gray) and high (red) setpoint forces from at least three replicates.

Figure 3 – source data 1. Size and height of molecular clusters.

FCHo2 forms ring-like shape assemblies on flat membranes

To establish the biogenesis of FCHo2 clusters at the molecular level, we used high-speed AFM (HS-AFM). Real-time imaging of the initial stages revealed the entire molecular process of FCHo2 cluster formation, from the binding of single FCHo2 homodimers to the growth of molecular clusters (Figure 4A). Representative time-lapse images and kymograph analysis along the dashed region at t = 0 s showed that the binding of individual FCHo2 proteins engages an indentation of few nm in the lipid membrane adjacent to the protein surface (Figure 4B, green arrowheads), as delineated from the cross-

section profile along the red dashed box in the corresponding kymograph (Figure 4A). The binding of FCHo2 rapidly prompted by the arrival of additional FCHo2 homodimers (as highlighted by white arrowheads in the kymograph). This stage of the process was characterized by minimal lateral interactions and the existence of contacts between adjacent FCHo2 homodimers, ultimately leading to a ring-like organization (Figure 4C and Figure 4-figure supplement 1). This dynamic reorganization that we named the "ring formation" step spanned over ~ 80-100 s.

The identification of individual proteins at the initial stages allowed us to extract the average dimension of the full-length protein interacting with the flat membrane, which was ~ 32 ± 8 nm (Figure 4D) and in good agreement with the size of the F-BAR domain reported from electron microscopy micrographs(10). After the ring formation, we observed the growth of FCHo2 clusters through docking events that involved individual FCHo2 homodimers and the coalescence of adjacent FCHo2 rings (Figure 4A, white arrowheads). FCHo2 self-organization into hollow ring-like assemblies was particularly discernible at the growth front of FCHo2 molecular clusters (Figure 4E and magnified image). Although the entire formation of FCHo2 molecular clusters expanded over few tens of minutes, we found that the docking of individual proteins and rings to support the expansion of the cluster took place every ~ 115 ± 94 s (Figure 4F). Collectively, our results suggest that on flat membranes, FCHo2 exhibits an intrinsic ability to self-assemble into a ring-like shape molecular complex independently of the local protein density.

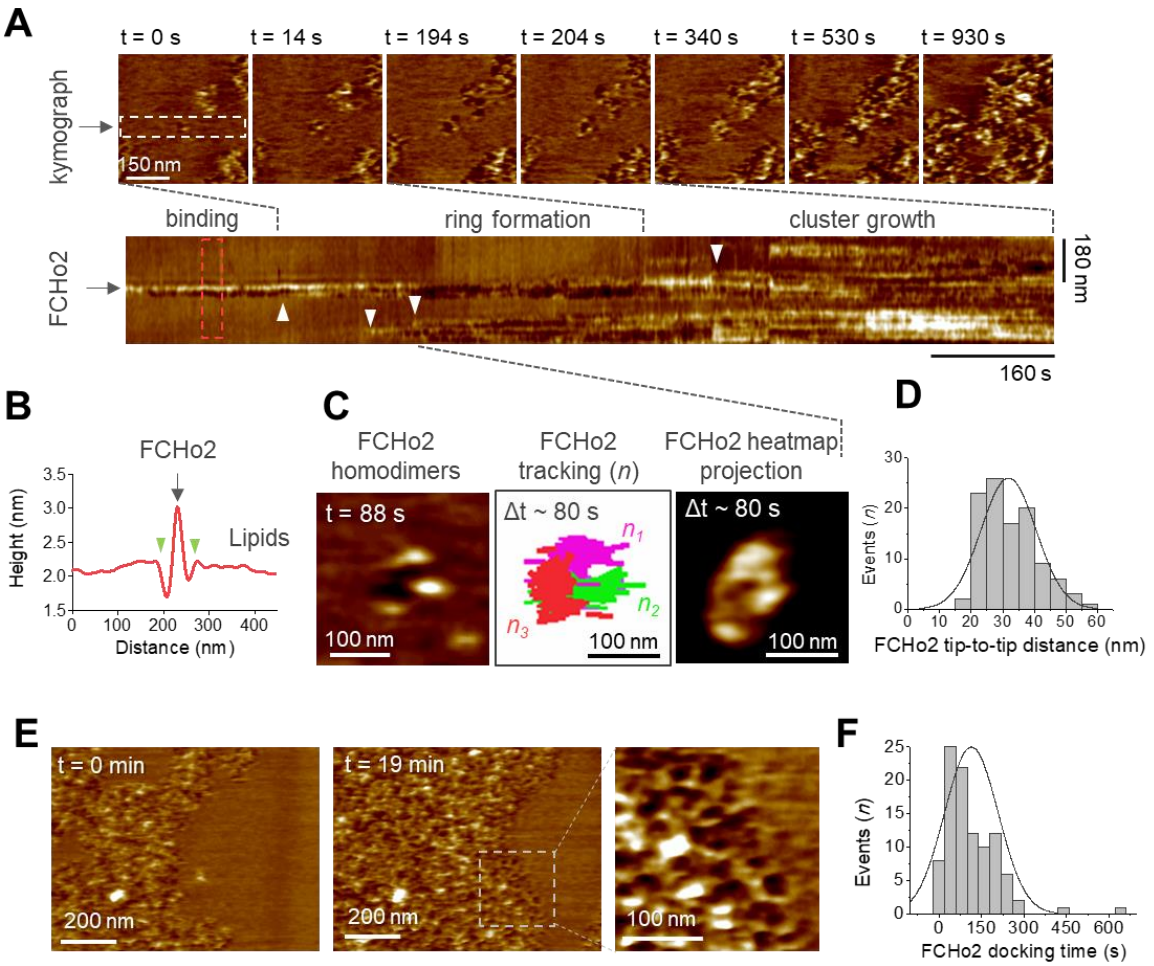

Figure 4. Molecular dynamics of FCHo2 self-assembly on PI(4,5)P_2-containing membranes. (A) HS-AFM movie frames of the binding of FCHo2 on 5% mol PI(4,5)P_2-containing membranes. Kymograph analysis performed on the white outline to display the representative stages of FCHo2 binding and self-assembly on flat membranes. White arrowheads highlight the docking of new FCHo2 homodimers to the growing molecular cluster. (B) Profile analysis along the red outline in A. Green arrowheads highlight the membrane invagination upon binding of FCHo2 on lipid membranes. (C) HS-AFM movie snapshot of the FCHo2 ring formation along with a representative tracking of individual homodimers (n = 3) and the heat map projection within a time interval, Δt, of ~ 80 s. (D) Size distribution (in nm) estimated from individual FCHo2 proteins before the cluster growth (t ≤ 200 s). (E) HS-AFM snapshots (t = 0 min and t = 19 min) illustrating the growth of FCHo2 molecular clusters into ring-like shape protein patches. Magnified image corresponds to the dashed outline. (F) Distribution of the docking time (in s) of individual and ring-like FCHo2 assemblies during the cluster growth from at least three replicates.

Figure 4 – source data 1. FCHo2 distance and docking time.

PI(4,5)P_2 assists FCHo2 partitioning on curved membranes

Because the transition from a flat surface to a dome-like invagination is a major step in the formation of clathrin-coated structures(2), we set out to monitor the organization of FCHo2 on curved

membranes. To this end, we engineered arrays of SiO_2 vertical nano-domes of radii R ~ 150 nm using soft nano-imprint lithography (soft-NIL) (Figure 5A), as previously reported(26). We functionalized SiO_2 nano-patterned substrates with supported lipid bilayers containing 20% of negatively charged lipids. Curvature sensing abilities of F-BAR proteins rely on hydrophobic insertion motifs, as in the case of syndapin1(27), or intrinsically disordered regions (IDR) as reported for FBP17(28). Indeed, the F-BAR domain of FBP17 displays minimal curvature sensing properties *in vitro* as compared to its IDR. Thus, we determined by airyscan microscopy the surface organization of the F-BAR domain and full-length FCHo2 labeled with Alexa647 on nano-domes in the presence of lipid bilayers containing 5% mol of PI(4,5)P_2 (Figure 5B). The three-dimensional (3D) rendering of the protein signal relative to a reference marker to depict the nano-dome topography (DHPE lipid, in gray), showed that while the F-BAR domain is excluded from the nano-structure, the FCHo2 staining is well present at the base of the nano-dome (Figure 5B). We hypothesize that if the association of FCHo2 with PI(4,5)P_2 is essential for its localization on curved membranes, disrupting this interaction would change its spatial organization. Indeed, this was the case, and replacing PI(4,5)P_2 by PS (20% mol PS) lead to the complete distribution of FCHo2 all over the nano-dome surface (Figure 5B, yellow).

To determine the precise localization of FCHo2 on nano-domes, we performed airyscan acquisitions at two z planes, at the top of the nano-dome and the bottom, according to the z-axis resolution of the setup (~ 0.35 µm)(29) (Figure 5C). First, we determined whether the distribution of PI(4,5)P_2 on the nano-domes was homogeneous. To this end, we monitored the axial localization of the PI(4,5)P_2 signal relative to the DHPE lipid dye on nano-domes coated with 5% PI(4,5)P_2-containing lipid bilayer (Figure 5C). The cross-section analysis showed an equivalent surface distribution of the PI(4,5)P_2 and DHPE lipid dye under our experimental conditions. Second, to confirm that TF-TMR-PI(4,5)P_2 signal was replicating the actual organization of the total pool of PI(4,5)P_2 on nano-domes, we analyzed the distribution of the PH domain of PLCδ1 PH(PLCδ1), which is a well-established reporter of PI(4,5)P_2(30). As expected, we obtained a homogenous distribution of the PH(PLCδ1), as indicated by the detection of the domain signal both on the flat surface (bottom plane) and all over the nano-dome structure (top plane) (Figure 5D). Following the same rationale, we monitored the surface localization of the F-BAR and extended F-BAR-x domains, and FCHo2 relative to DHPE, as a reference of the nano-dome height. On nano-domes functionalized with PI(4,5)P_2-containing membranes, the F-BAR and F-BAR-x preferentially bind to the flat surface and appear absent from the nano-dome structure (Figure 5E-F, green and orange). Whereas FCHo2 revealed a preferential accumulation at the base of the nano-dome (Figure 5E-F, magenta). Finally, in the presence of PS membranes, FCHo2 was no longer accumulated at the edges of nano-domes and displayed a homogenous distribution (Figure 5E-F, yellow). Collectively, these data suggest that the F-BAR domain of FCHo2 displays minimal sensing of curvatures of radii ~ 150 nm *in vitro* and that PI(4,5)P_2-mediated accumulation of FCHo2 at the rims of nano-domes is likely to originate *via* its downstream protein regions (i.e., the disordered

central region(13) and C-terminal μ-HD(8, 9)), in agreement with the curvature-sensing profile reported for the F-BAR domain protein FBP17(28).

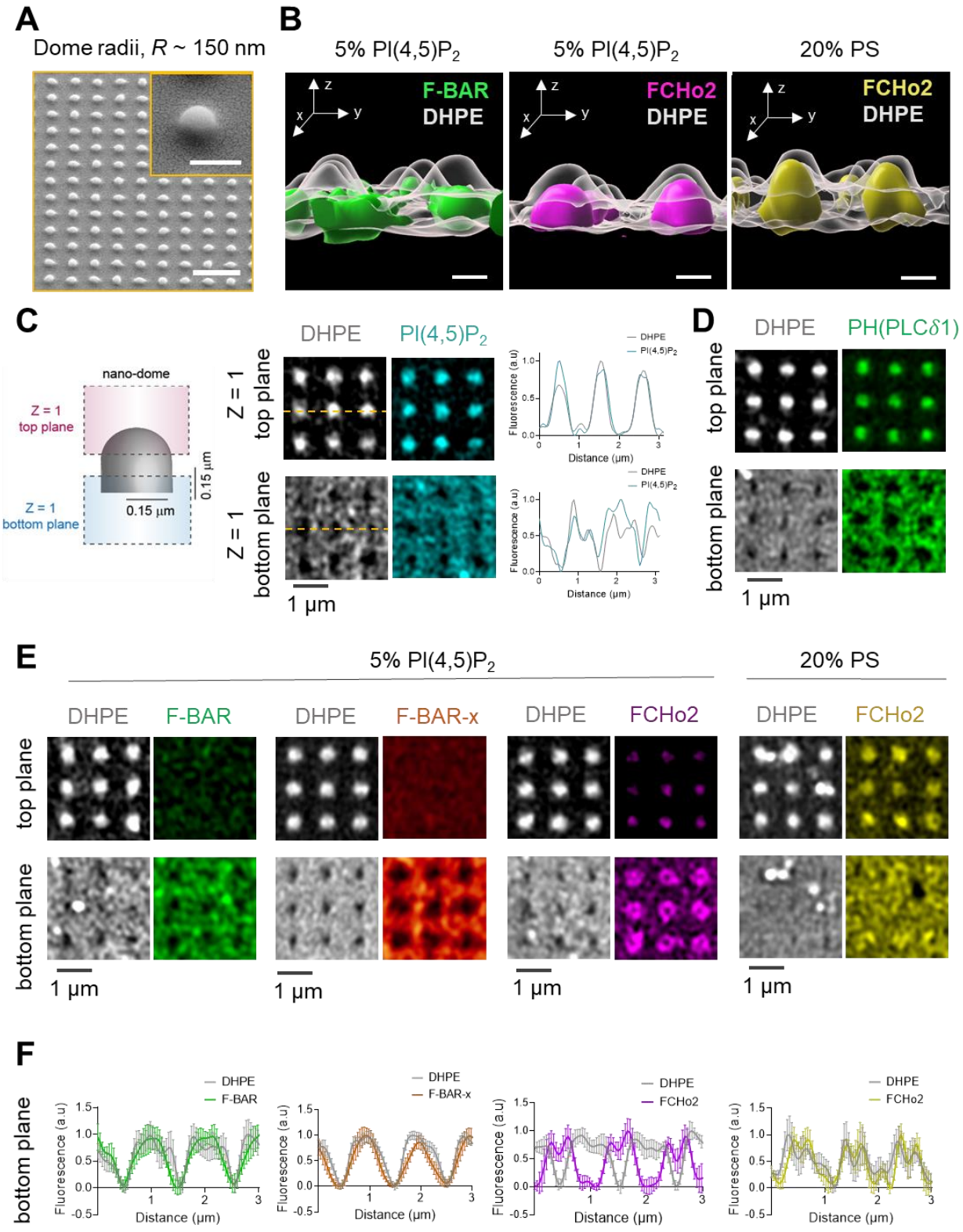

Figure 5. PI(4,5)P_2 assists the organization of FCHo2 on curved membranes. (A) SEM images of SiO_2 substrates displaying an array of nano-domes with a radius, R ~ 150 nm generated by soft-NIL. Scale bar, 2 µm. Inset, scale bar is 500 nm. (B) Representative 3D renders of the surface organization of the F-BAR domain (green) and FCHo2 (magenta) on nano-domes functionalized with either 5% mol PI(4,5)P_2 or 20% PS-containing membranes (yellow) relative to the DHPE lipid dye signal (grey). Scale bar, 400 nm. (C) *Left*, schematic representation of the acquisition of a single plane (Z = 1) at the top and bottom of nano-domes to visualize the preferential distribution of proteins. *Right*, representative airyscan images showing the surface distribution of fluorescent DHPE (gray) and PI(4,5)P_2 (cyan) on nano-domes along with a cross-section (orange dashed line) of the normalized fluorescence intensity of DHPE (gray) and PI(4,5)P_2 (cyan) at the top and bottom of the nano-dome. (D) Representative airyscan images showing the surface distribution of the PH (PLCδ1) domain (green) on nano-domes functionalized with 5% mol of PI(4,5)P_2. (E-F) Representative airyscan images (E) and average profile analysis of the normalized fluorescence intensity (F) showing the surface distribution of fluorescent DHPE (gray) and F-BAR (green), F-BAR-x (orange) and FCHo2 (magenta) on PI(4,5)P_2-containing membranes and FCHo2 (yellow) on PS-containing membranes at the bottom of nano-domes. Each curve represents the mean ± s.d. of n = 20 nano-domes from at least three replicates.

Discussion

This study reports a molecular visualization of the docking and self-assembly of the endocytic protein FCHo2 on *in vitro* and cellular membranes (Figure 5). Our results show that PI(4,5)P_2 is a primary spatial regulator of the recruitment of FCHo2 by promoting its accumulation and sorting on flat and curved membranes (Figure 1 and Figure 5). These observations support the model that, in addition to protein-protein interactions(13), multivalent lipid-protein interactions play an instrumental role in upholding the early stages of endocytosis. Furthermore, we show that, in the absence of ATP, FCHo2 oligomerization induces PI(4,5)P_2 clustering formation on cellular membranes that are often co-localized with TfR and EGFR-positive puncta (Figure 1). This association was particularly remarkable in the case of the EGFR and agreed with the observation that electrostatic interaction of the polybasic motifs at the cytoplasmic tail of the EGFR mediates its clustering on PI(4,5)P_2-enriched domains(15, 21, 31). As previously reported, FCHo1/2 is needed to recruit Eps15(7) and form FCHo1/2-Eps15 micrometer-scale domains on membranes(13). By driving PI(4,5)P_2 clustering formation at the boundary of cargo receptors, FCHo2 is likely to improve the stability of a network of PI(4,5)P_2-interacting proteins through avidity(32). Indeed, the F-BAR domain alone was reported to facilitate local PI(4,5)P_2 accumulation and our observations confirm a 1.4-fold increase in the formation of clathrin-positive assemblies on *in vitro* membranes (Figure 2). This effect is intensified by the coupled action of membrane tubulation and the APA domain, possibly *via* AP2 activation, in agreement with previous studies pointing that clustering of Fcho1/2Eps15/AP2 primes endocytosis(8, 23). Furthermore, we discerned clathrin-positive puncta in lower FCHo2 concentrations but not in PI(4,5)P_2-depleted membranes, which agrees with the observation that AP2 can create its local pool of PI(4,5)P_2(22), although it requires PI(4,5)P_2 for its localization and activation at the plasma membrane(33, 34). Thus, our measurements point that local PI(4,5)P_2 enrichment induced by FCHo2

might operate as a complementary and/or synergistic mechanism to PI(4,5)P_2 synthesis on promoting pre-endocytic events (Figure 1 and 2).

This work provides the first evidence that FCHo2 self-assembles into ring-like molecular complexes on flat lipid bilayers (Figure 3 and 4) and supports the observation of FCHo2 rings at the rims of nascent clathrin-coated structures in living cells(23). This singular organization agrees with a side-lying conformation proposed for F-BAR scaffolds at low protein densities on flat surfaces(10) and the partitioning of FCHo1/2 at the edges of flat clathrin lattices(35). HS-AFM movies show that the ring formation process is relatively fast and takes place within less than 100 s (Figure 4), which is compatible with the temporal scales reported during clathrin-coat assembly(1). Previous works reported that lateral contacts stabilize the self-assembly of F-BAR domains on membrane tubules(10, 36) and our investigations point out that this type of interaction might also occur on flat surfaces. We observed the anisotropic growth and formation of FCHo2 molecular clusters in the absence of other endocytic proteins and, importantly, show that F-BAR proteins can moderately bend flat membranes at high protein densities.

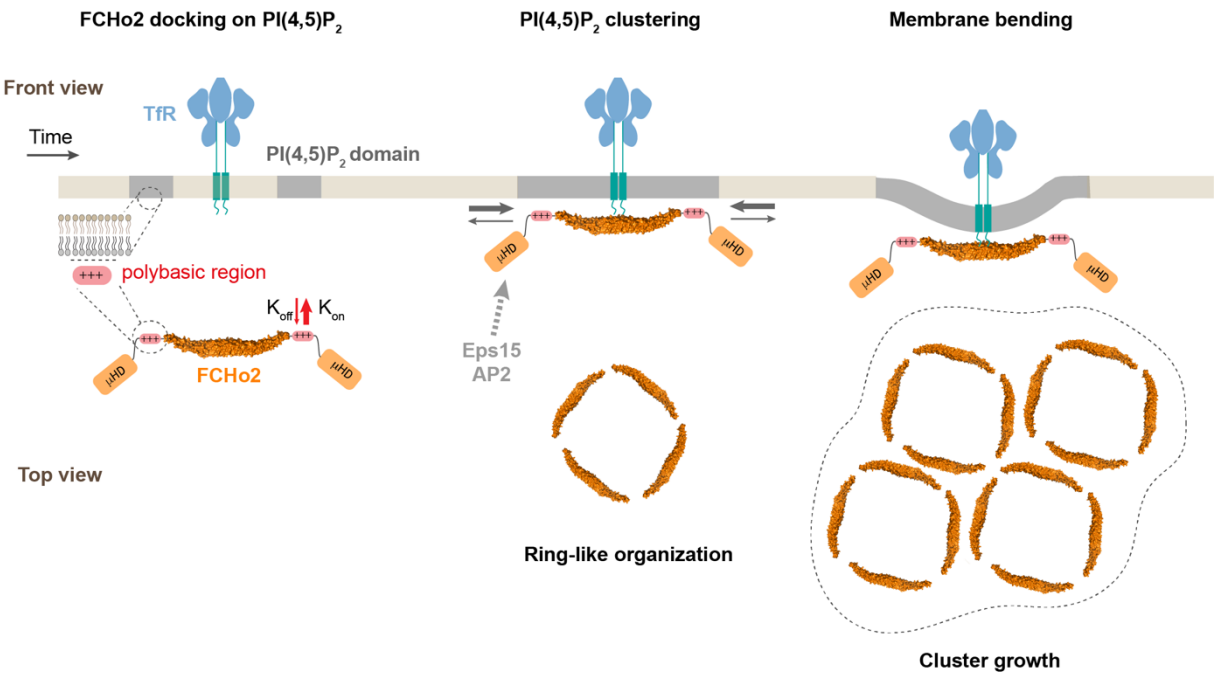

Figure 5. Model of FCHo2 docking and self-assembly on membranes. FCHo2 recruitment of membranes is mediated by PI(4,5)P_2. Increase in the local PI(4,5)P_2 concentration enhances the spatial accumulation of FCHo2 through multivalent interactions between the positively charged surface of the F-BAR domain and polybasic region with PI(4,5)P_2 molecules. Binding of FCHo2 on cellular membranes is convoyed by PI(4,5)P_2 clustering formation at the boundary of clathrin-regulated cargo receptors and the self-assembly of FCHo2 into a ring-like shape protein complex. As a result of this singular organization, the local accumulation of PI(4,5)P_2 and APA/μHD of FCHo2 is likely to facilitate the formation of an

interacting network with downstream partners, such as Eps15 and AP2(7, 8), ultimately leading to the assembly of clathrin structures on a PI(4,5)P_2-rich interface that could be amplified by phosphoinositides metabolizing enzymes(3). In the absence of endocytic partners, FCHo2 rings grow into sub-micrometric molecular clusters leading to membrane bending and the partitioning on curved membranes.

Conclusions

In conclusion, our study provides a molecular picture of the recruitment and self-assembly of the early endocytic protein FCHo1/2 on membranes. We found that the binding of FCHo2 on cellular membranes promotes the local accumulation of PI(4,5)P_2 at the vicinity of clathrin-regulated cargo receptors. As a result, in the absence of phosphoinositides-metabolizing enzymes, FCHo2 can enhance the formation of clathrin structures through PI(4,5)P_2-rich interfaces, which could explain previous studies showing that FCHo1/2 depletion slows down the progression of cargo-loaded clathrin structures (8, 9, 12, 37). Because FCHo1/2 is among the first proteins recruited at endocytic sites, the discovery that FCHo2 self-assembles into rings convoyed by local PI(4,5)P_2 accumulation and membrane bending provides a fundamental understanding of the initiating mechanism of clathrin-mediated endocytosis(2, 23).

Materials and Methods

Lipids and reagents

Natural and synthetic phospholipids, including POPC, POPS, Egg-PC, Brain-PS, Brain-PI(4,5)P_2, and fluorescent TopFluor-TMR-PI(4,5)P_2 and TopFluor-TMR-PS are from Avanti Polar Lipids, Inc. Oregon green 488-DHPE and Alexa Fluor 647 Maleimide labelling kit are from Invitrogen. Atto647N-DOPE was from Sigma. Monoclonal mouse anti-clathrin heavy chain (dilution 1:1000; Cat. Nr. 610499) was from BD Biosciences and polyclonal rabbit anti-FCHo2 (dilution 1:1000; Cat. Nr. NBP2-32694) was from Novusbio.

Mammalian cell line

HT1080 cells were kindly provided by Dr. N. Arhel, IRIM, CNRS UMR9004, Montpellier, France. Cell lines were verified to be free of mycoplasma contamination and the identities were authenticated by short tandem repeat (STR) profiling (Eurofins Genomics).

EGFR-GFP and TfR-GFP stable cell lines

pRRL.sin.cPPT.SFFV-EGFP/IRES-puro was kindly provided by C. Goujon (IRIM, CNRS UMR9004, Montpellier, France), the EGFR-GFP vector was a gift from Alexander Sorkin, (Addgene plasmid #32751) and the pBa.TfR.GFP vector was a gift from Gary Banker & Marvin Bentley (Addgene plasmid # 4506). The GFP was replaced by a GFP-delta-ATG using these primers: 5'-gtatatatatGGATCCGTGAGCAAGGGCGAGGAG-3' and 5'-CTCACATTGCCAAAAGACG-3'. GFP-delta-ATG fragment replaced the GFP- fragment in pRRL.sin.cPPT.SFFV-EGFP/IRES-puro using a BamHI-XhoI digestion. EGFR was amplified with these primers: 5'-caaatatttgcggccgcATGCGACCCTCCGGGACG-3' and 5'-gtataccggttgaacctccgccTGCTCCAATAAATTCACTGCTTTGTGG-3' and cloned into pRRL.sin.cPPT.SFFV-EGFP-delta-ATG/IRES-puro using NotI-AgeI to generate a fused EGFR-GFP protein.

Lentiviral vector stocks were obtained by polyethylenimine (PEI)-mediated multiple transfection of 293T cells in 6-well plates with vectors expressing Gag-Pol (8.91), the mini-viral genome (pRRL.sin.cPPT.SFFV-EGFR-GFP/IRES-puro) and the Env glycoprotein of VSV (pMD.G) at a ratio of 1:1:0.5. The culture medium was changed 6 hr post-transfection and lentivectors containing supernatants harvested 48 hr later, filtered and stored at -80°C.

The mini-viral genome (pRRL.sin.cPPT.SFFV-TFR-GFP/IRES-puro) and the corresponding lentivectors were generated as detailed in the case of the EGFR-GFP.

To generate a stable cell line HT1080 expressing EGFR-GFP or TfR-GFP, HT1080 cells were transduced in 6-well plates using the supernatant of one 6-well plates of the lentiviral stock production detailed above. The culture medium was changed 6 hr post-transduction. Puromycin (1µg/ml) was added 48h after transduction. The percentage of GFP-expressing cells was enumerated by flow cytometry 72 hr after selection under puromycin.

HT1080 cells constitutively expressing the EGFR-GFP or TfR-GFP were cultured in DMEM GlutaMAX supplemented with 10% fetal calf serum, 100 $U \cdot mL^{-1}$ of penicillin and streptomycin and 1µg·ml^{-1} of puromycin at 37ºC in 5%CO_2. Cell lines were tested negative for mycoplasma.

Protein purification and protein labeling

pGEX-6P-1 vector coding for the mouse full-length FCHo2 (aa 1-809), F-BAR domain (aa 1-262) and F-BAR-x (aa 1-430) were obtained from H.T McMahon (MRC Laboratory of Molecular Biology, Cambridge, UK). Proteins were subcloned into a pET28a vector with a PreScission protease cleaving site. Proteins were expressed in BL21(DE3) bacteria and purified by affinity chromatography using a HiTrap™ chelating column (GE Healthcare) according to the manufacturer's instructions in 50 mM Tris at pH 8.0, 100 mM NaCl. Proteins were expressed overnight at 18°C using 1 mM IPTG. Proteins

were then dialyzed overnight in a Slide-A-Lyzer dialysis cassette (MWCO 10,000) before Alexa Fluor 647 maleimide labelling following the protocol described by the manufacturer (Invitrogen). Protein concentrations were measured using a Bradford assay (Biorad).

Recombinant GST-eGFP-PH-domain (PLCδ1) detecting $PI(4,5)P_2$ was purified as described in(26).

Xenopus *laevis* egg extracts

Laid eggs are rinsed twice in XB Buffer (100mM KCl, 1mM MgCl2, 0.1mM CaCl2, 50mM sucrose and 10mM HEPES at pH 7.7) and subsequently dejellied with 2% cysteine solution pH7.8. Once dejellied they are extensively rinsed with XB buffer to completely eliminate cysteine solution.

Eggs are then recovered from a Petri dish and treated with Ca2+ Ionophore (final concentration 2 µg/ml) and 35 minutes later, they are crushed by centrifugation for 20min at 10,000g at 4°C. The cytoplasmic layer is collected and supplemented with Cytochalasin B (50ug/ml) Aprotinin (5ug/ml), Leupeptin (5ug/ml) and 10 mM Creatin Phosphate. Cytoplasmic extract is centrifuged again for 20 min at 10,000g. Extract are frozen and then used as described in Figure 2.

The energy mix consisted of 1.5 mM ATP, 0.15 mM GTPγS, 16.7 mM creatine phosphate and creatine phosphokinase 16.7 $U \cdot ml^{-1}$, as previously reported(38).

Supported lipid bilayers

Lipid mixtures consisted of: 80-85% Egg-PC, 10-15% Brain-PS and 5-10% of Brain-$PI(4,5)P_2$. The amount of total negatively charged lipids was kept to 20% for any of the mixtures containing phosphoinositides at the expenses of Brain-PS. If needed, fluorescent lipids were added to 0.2%.

For fluorescence microscopy experiments, supported lipid bilayers were prepared as described in(39). Experiments were performed by injecting 20 µL of buffer (20 mM Tris, pH 7.4, 150 mM NaCl and 0.5 $mg \cdot ml^{-1}$ of casein). Supported lipid bilayers were imaged on a Zeiss LSM880 confocal microscope.

For HS-AFM experiments, supported lipid bilayers were prepared following the method described in(40). Briefly, large unilamellar vesicles (LUVs, diameter ~ 100 nm) were obtained by extrusion of multilamellar vesicles of 85% POPC, 10% POPS and 5% Brain-$PI(4,5)P_2$ in 20 mM Hepes, pH 7.4, 150 mM NaCl. LUVs were supplemented with 20 mM of $CaCl_2$ and deposited onto freshly cleaved mica disks. Samples were incubated for 20 min at 60 °C and extensively rinsed with 20 mM Hepes, pH 7.4, 150 mM NaCl, 20 mM EDTA. Finally, bilayers were rinsed and keep under the imaging buffer, 20 mM Hepes, pH 7.4, 150 mM NaCl.

Plasma membrane sheets

Unroofing of HT1080 cells stably expressing the EGFR-GFP was performed by tip sonication as reported in(41). Cells were rinsed three times in cold Ringer buffer supplemented with Ca^{2+} (155mM NaCl, 3 mM KCl, 3mM $NaH2PO_4$, 5mM HEPES, 10mM glucose, 2 mM $CaCl_2$, 1mM $MgCl_2$, pH 7.2), then immersed 10 s in Ca^{2+}-free Ringer buffer containing 0.5 $mg \cdot mL^{-1}$ poly-L-lysine. Cells were unroofed by scanning the coverslip with the tip sonicator at 10% of power under HKMgE buffer consisting of 70 mM KCl, 30mM HEPES, 5 mM $MgCl_2$, 3mM EGTA, pH 7.2. Unroofed cells were kept in HKMgE buffer. Fluorescent labeling of plasma membrane sheets was performed immediately after unroofing by incubating the sample with 100 nmol of TopFluor-TMR-PtdIns(4,5)P_2 suspended in 0.2% of absolute ethanol during 5 min, as reported in(42). Then, samples were extensively rinsed with HKMgE buffer and immediately imaged under the Zeiss LSM880 confocal microscope. Before addition of 1 µM of FCHo2-Alexa647, unroofed cells were rinsed with HKMgE buffer supplemented with 0.5 $mg \cdot ml^{-1}$ of casein.

Immunofluorescence

Supported lipid bilayers were fixed in 3.2% PFA in PBS for 2 min at room temperature, then rinsed in PBS twice. Samples were stained for the primary antibody for 45 min at room temperature in 1% BSA. Then, the secondary antibody was incubated for 45 min.

HT1080 cells were transfected with either pmCherry-C1 (empty vector), FCHo1-pmCherryC1 or FCHo2-pmCherryC1 using Lipofectamine 2000 (ThermoFisher) according to the manufacturer's instructions. Then, plasma membrane staining of endogenous PI(4,5)P_2 was performed as described in(43). Briefly, cells were fixed on ice with 3.7% formaldehyde and 0.2% glutaraldehyde for 15 min. After three washes with NH_4Cl, cells were incubated for 1 hour in blocking buffer (PIPES-BS, NH4Cl 50mM, 1% lipid-free BSA, Saponin 0.05%), then incubated for two hours with recombinant GST-eGFP-PH-domain (PLCδ1) probe against PI(4,5)P_2 in PIPES-BS, 1% lipid-free BSA, Saponin 0.1% on ice. After three washes with PIPES-BS for 5 min, cells were incubated with 3.7% formaldehyde for 10 min, then 5 min at room temperature.

Finally, all samples were extensively rinsed in PBS, then in sterile water and mounted with a Mowiol® 4-88 mounting medium (Polysciences, Inc.). Montage was allowed to solidify in the dark for 48 h before microscope acquisitions.

Silica thin film nanostructuration

SiO_2 vertical nanostructures were prepared on conventional borosilicate coverslips with precision thickness No. 1.5 (0.170 ± 0.005 mm), as previously reported(26, 44). Briefly, Si masters were

elaborated using LIL Lithography as detailed in(44, 45). PDMS (polydimethylsiloxane) reactants (90 w% RTV141A; 10 w% RTV141B from BLUESIL) were transferred onto the master and dried at 70 °C for 1 h before unmolding.

Silica precursor solution was prepared by adding 4.22 g tetraethyl orthosilicate (TEOS) into 23.26 g absolute ethanol, then 1.5 g HCl (37%), and stirring the solution for 18 h. The final molar composition was TEOS:HCl:EtOH=1:0.7:25. All the chemicals were from Sigma. Gel films were obtained by dip-coating the coverslips with a ND-DC300 dip-coater (Nadetech Innovations) equipped with an EBC10 Miniclima device to control the surrounding temperature and relative humidity to 20ºC and 45-50%, respectively. The thickness of film was controlled by the withdrawal rate at 300 mm/min. After dip-coating, gel films were consolidated at 430ºC for 5 min. Then, a new layer of the same solution was deposited under the same conditions for printing with the PDMS mold. After imprinting, the samples were transferred to a 70 °C oven for 1 min and then to a 140 °C for 2 min to consolidate the xerogel films before peeling off the PDMS mold. Finally, the sol–gel replicas were annealed at 430 °C for 10 min for consolidation.

Fluorescence microscopy

Images were acquired on a Zeiss LSM880 Airyscan confocal microscope (MRI facility, Montpellier). Excitation sources used were: 405 nm diode laser, an Argon laser for 488 nm and 514 nm and a Helium/Neon laser for 633 nm. Acquisitions were performed on a 63x/1.4 objective. Multidimensional acquisitions were acquired via an Airyscan detector (32-channel GaAsP photomultiplier tube (PMT) array detector). 3D images were acquired by fixing a 0.18 µm z-step depth, according to the recommendations of the acquisition setup.

HS-AFM imaging

HS-AFM movies were acquired with an HS-AFM (SS-NEX, Research Institute of Biomolecule Metrology, Tsukuba, Japan) equipped with a superluminescent diode (wavelength, 750 nm; EXS 7505-B001, Exalos, Schlieren, Switzerland) and a digital high-speed lock-in Amplifier (Hinstra, Transcommers, Budapest, Hungary)(46) following the protocol detailed at(47). Scanning was performed using USC-1.2 cantilevers featuring an electron beam deposition tip (NanoWorld, Neuchâtel, Switzerland) with a nominal spring constant k = 0.15 N/m, resonance frequency f(r) = 600 kHz, and quality factor Qc ≈ 2 under liquid conditions. For high-resolution imaging, the electron beam deposition tip was sharpened by helium plasma etching using a plasma cleaner (Diener Electronic, Ebhausen, Germany). Images were acquired in amplitude modulation mode at the minimal possible applied force that enables good quality of imaging under optical feedback parameters.

Image processing and quantification

Line profiles of the fluorescence intensities were done using ImageJ(48) and the kymographs were made using the Kymograph plugin (http://www.embl.de/eamnet/html/body_kymograph.html).

Protein binding was quantified by measuring the mean grey value of the protein channel that was then normalized by the mean gray value of the membrane intensity (as indicated by the TF-TMR-PI(4,5)P_2 fluorescence) in the same image. Mean gray values were measured once protein binding reached the steady-state, which was estimated from the binding kinetics to be < 4 min. Protein binding was averaged from 3 experimental replicates. Mean gray values were measured using ImageJ. Concentrations and confocal parameters were kept constant between experiments and samples.

The automatic analysis of images to determine molecular clusters was performed with ImageJ(48). Spots of different sizes are detected using a scale space spot detection (49) and overlapping spots are merged. The LoG filter of the FeatureJ plugin(50) is used to create the scale space. Starting points are detected as local minima of the minimum projection and as minima on the smallest scale. A simplified linking scheme is applied that looks for minima along the scales for each starting point within the radius of the spot on the given scale. Two spots are merged if at least 20 percent of the surface of one spot is covered by the other. The noise tolerance for the spot detection is determined manually for each series of input images.

HS-AFM images were processed using Gwyddion, an open-source software for SPM data analysis, and WSxM(51).

Data representation and statistical analysis

Representation of cross-section analysis and recruitment curves was performed using Origin software. 3D rendering of Airyscan images was generated with the 3/4D visualization and analysis software Imaris (Oxford Instruments).

Statistical analysis was performed using the two-tailed, unpaired Welch's t test, or ordinary one-way ANOVA and Dunnett's multiple comparisons test, with single pooled variance using Prism GraphPad software. In all statistical, the levels of significance were defined as: *P<0.05, **P<0.01, ***P<0.001 and ****P<0.0001.

References

1. M. J. Taylor, D. Perrais, C. J. Merrifield, A High Precision Survey of the Molecular Dynamics of Mammalian Clathrin-Mediated Endocytosis. *PLoS Biol* **9**, e1000604 (2011).

2. V. Haucke, M. M. Kozlov, Membrane remodeling in clathrin-mediated endocytosis. *J Cell Sci* **131**, jcs216812 (2018).

3. Y. Posor, M. Eichhorn-Grünig, V. Haucke, Phosphoinositides in endocytosis. *Biochimica et Biophysica Acta (BBA) - Molecular and Cell Biology of Lipids* **1851**, 794–804 (2015).

4. G. J. Doherty, H. T. McMahon, Mechanisms of Endocytosis. *Annu. Rev. Biochem.* **78**, 857–902 (2009).

5. M. P. Sheetz, Cell control by membrane–cytoskeleton adhesion. *Nat Rev Mol Cell Biol* **2**, 392–396 (2001).

6. C. Godlee, M. Kaksonen, From uncertain beginnings: Initiation mechanisms of clathrin-mediated endocytosis. *J Cell Biol* **203**, 717–725 (2013).

7. W. M. Henne, *et al.*, FCHo Proteins Are Nucleators of Clathrin-Mediated Endocytosis. *Science* **328**, 1281–1284 (2010).

8. L. Ma, *et al.*, Transient Fcho1/2·Eps15/R·AP-2 Nanoclusters Prime the AP-2 Clathrin Adaptor for Cargo Binding. *Developmental Cell* **37**, 428–443 (2016).

9. G. Hollopeter, *et al.*, The membrane-associated proteins FCHo and SGIP are allosteric activators of the AP2 clathrin adaptor complex. *eLife* **3**, e03648 (2014).

10. A. Frost, *et al.*, Structural Basis of Membrane Invagination by F-BAR Domains. *Cell* **132**, 807–817 (2008).

11. W. M. Henne, *et al.*, Structure and Analysis of FCHo2 F-BAR Domain: A Dimerizing and Membrane Recruitment Module that Effects Membrane Curvature. *Structure* **15**, 839–852 (2007).

12. P. K. Umasankar, *et al.*, Distinct and separable activities of the endocytic clathrin-coat components Fcho1/2 and AP-2 in developmental patterning. *Nat Cell Biol* **14**, 488–501 (2012).

13. K. J. Day, *et al.*, Liquid-like protein interactions catalyse assembly of endocytic vesicles. *Nat Cell Biol* **23**, 366–376 (2021).

14. J. P. Zewe, *et al.*, Probing the subcellular distribution of phosphatidylinositol reveals a surprising lack at the plasma membrane. *Journal of Cell Biology* **219** (2020).

15. H. Koldsø, D. Shorthouse, J. Hélie, M. S. P. Sansom, Lipid Clustering Correlates with Membrane Curvature as Revealed by Molecular Simulations of Complex Lipid Bilayers. *PLoS Comput Biol* **10**, e1003911 (2014).

16. T. Itoh, *et al.*, Dynamin and the Actin Cytoskeleton Cooperatively Regulate Plasma Membrane Invagination by BAR and F-BAR Proteins. *Developmental Cell* **9**, 791–804 (2005).

17. A. Honigmann, *et al.*, Phosphatidylinositol 4,5-bisphosphate clusters act as molecular beacons for vesicle recruitment. *Nat Struct Mol Biol* **20**, 679–686 (2013).

18. G. van den Bogaart, *et al.*, Membrane protein sequestering by ionic protein–lipid interactions. *Nature* **479**, 552–555 (2011).

19. H. Zhao, *et al.*, Membrane-Sculpting BAR Domains Generate Stable Lipid Microdomains. *Cell Reports* **4**, 1213–1223 (2013).

20. L. Picas, *et al.*, BIN1/M-Amphiphysin2 induces clustering of phosphoinositides to recruit its downstream partner dynamin. *Nat Commun* **5**, 5647 (2014).

21. Y. Wang, *et al.*, Regulation of EGFR nanocluster formation by ionic protein-lipid interaction. *Cell Res* **24**, 959–976 (2014).

22. M. Krauss, V. Kukhtina, A. Pechstein, V. Haucke, Stimulation of phosphatidylinositol kinase type I-mediated phosphatidylinositol (4,5)-bisphosphate synthesis by AP-2 -cargo complexes. *Proceedings of the National Academy of Sciences* **103**, 11934–11939 (2006).

23. M. Lehmann, *et al.*, Nanoscale coupling of endocytic pit growth and stability. *Sci. Adv.* **5**, eaax5775 (2019).

24. A. Walrant, D. S. Saxton, G. P. Correia, J. L. Gallop, "Triggering actin polymerization in Xenopus egg extracts from phosphoinositide-containing lipid bilayers" in *Methods in Cell Biology*, (Elsevier, 2015), pp. 125–147.

25. F. Daste, *et al.*, Control of actin polymerization via the coincidence of phosphoinositides and high membrane curvature. *J. Cell Biol.* **216**, 3745–3765 (2017).

26. T. Sansen, *et al.*, Mapping Cell Membrane Organization and Dynamics Using Soft Nanoimprint Lithography. *ACS Appl. Mater. Interfaces*, acsami.0c05432 (2020).

27. P. Ramesh, *et al.*, FBAR Syndapin 1 recognizes and stabilizes highly curved tubular membranes in a concentration dependent manner. *Sci Rep* **3**, 1565 (2013).

28. M. Su, *et al.*, Comparative Study of Curvature Sensing Mediated by F-BAR and an Intrinsically Disordered Region of FBP17. *iScience* **23**, 101712 (2020).

29. J. Huff, *et al.*, The new 2D Superresolution mode for ZEISS Airyscan. *Nat Methods* **14**, 1223–1223 (2017).

30. M. A. Lemmon, K. M. Ferguson, R. O'Brien, P. B. Sigler, J. Schlessinger, Specific and high-affinity binding of inositol phosphates to an isolated pleckstrin homology domain. *Proceedings of the National Academy of Sciences* **92**, 10472–10476 (1995).

31. K. B. Abd Halim, H. Koldsø, M. S. P. Sansom, Interactions of the EGFR juxtamembrane domain with PIP2-containing lipid bilayers: Insights from multiscale molecular dynamics simulations. *Biochimica et Biophysica Acta (BBA) - General Subjects* **1850**, 1017–1025 (2015).

32. Y. Chen, *et al.*, Dynamic instability of clathrin assembly provides proofreading control for endocytosis. *J. Cell Biol.* **218**, 3200–3211 (2019).

33. Z. Kadlecova, *et al.*, Regulation of clathrin-mediated endocytosis by hierarchical allosteric activation of AP2. *Journal of Cell Biology* **216**, 167–179 (2017).

34. S. Höning, *et al.*, Phosphatidylinositol-(4,5)-Bisphosphate Regulates Sorting Signal Recognition by the Clathrin-Associated Adaptor Complex AP2. *Molecular Cell* **18**, 519–531 (2005).

35. K. A. Sochacki, A. M. Dickey, M.-P. Strub, J. W. Taraska, Endocytic proteins are partitioned at the edge of the clathrin lattice in mammalian cells. *Nat Cell Biol* **19**, 352–361 (2017).

36. C. Mim, *et al.*, Structural Basis of Membrane Bending by the N-BAR Protein Endophilin. *Cell* **149**, 137–145 (2012).

37. E. E. Mulkearns, J. A. Cooper, FCH domain only-2 organizes clathrin-coated structures and interacts with Disabled-2 for low-density lipoprotein receptor endocytosis. *MBoC* **23**, 1330–1342 (2012).

38. M. Wu, *et al.*, Coupling between clathrin-dependent endocytic budding and F-BAR-dependent tubulation in a cell-free system. *Nat Cell Biol* **12**, 902–908 (2010).

39. J. A. Braunger, C. Kramer, D. Morick, C. Steinem, Solid Supported Membranes Doped with PIP_2: Influence of Ionic Strength and pH on Bilayer Formation and Membrane Organization. *Langmuir* **29**, 14204–14213 (2013).

40. L. Picas, *et al.*, Preferential insertion of lactose permease in phospholipid domains: AFM observations. *Biochimica et Biophysica Acta (BBA) - Biomembranes* **1798**, 1014–1019 (2010).

41. J. Heuser, The Production of 'Cell Cortices' for Light and Electron Microscopy. *Traffic* **1**, 545–552 (2000).

42. V. Mueller, *et al.*, STED Nanoscopy Reveals Molecular Details of Cholesterol- and Cytoskeleton-Modulated Lipid Interactions in Living Cells. *Biophysical Journal* **101**, 1651–1660 (2011).

43. W. E. Edimo, *et al.*, SHIP2 controls plasma membrane PI(4,5)P2 thereby participating in the control of cell migration in 1321 N1 glioblastoma. *Journal of Cell Science*, jcs.179663 (2016).

44. Q. Zhang, *et al.*, Micro/Nanostructure Engineering of Epitaxial Piezoelectric α-Quartz Thin Films on Silicon. *ACS Appl. Mater. Interfaces* **12**, 4732–4740 (2020).

45. Q. Zhang, *et al.*, Tailoring the crystal growth of quartz on silicon for patterning epitaxial piezoelectric films. *Nanoscale Adv.*, 10.1039.C9NA00388F (2019).

46. A. Colom, I. Casuso, F. Rico, S. Scheuring, A hybrid high-speed atomic force–optical microscope for visualizing single membrane proteins on eukaryotic cells. *Nat Commun* **4**, 2155 (2013).

47. F. Zuttion, L. Redondo-Morata, A. Marchesi, I. Casuso, "High-Resolution and High-Speed Atomic Force Microscope Imaging" in *Nanoscale Imaging: Methods and Protocols*, Methods in Molecular Biology., Y. L. Lyubchenko, Ed. (Springer, 2018), pp. 181–200.

48. C. A. Schneider, W. S. Rasband, K. W. Eliceiri, NIH Image to ImageJ: 25 years of image analysis. *Nat Methods* **9**, 671–675 (2012).

49. T. Lindeberg, *Scale-Space Theory in Computer Vision* (Springer US, 1994) https:/doi.org/10.1007/978-1-4757-6465-9 (October 14, 2020).

50. , FeatureJ (October 14, 2020).

51. I. Horcas, *et al.*, WSXM: A software for scanning probe microscopy and a tool for nanotechnology. *Review of Scientific Instruments* **78**, 013705 (2007).

Acknowledgements

The authors thank H.T. McMahon for kindly providing F-BAR domain protein constructs. C. Goujon and O. Moncorgé for helping in the transduction of HT1080 cells. C. Holuka for assistance with plasma membrane sheets. P. Maiuri for assistance in data analysis. J.B. Manneville for critical reading of the manuscript and discussion. S. Roche, C. Favard, and D. Muriaux for scientific discussions. We

acknowledge the imaging facility MRI, member of the national infrastructure France-BioImaging infrastructure supported by the French National Research Agency (ANR-10-INBS-04, «Investments for the future»). L.P. acknowledges the ATIP-Avenir program (AO-2016) and ANR-18-CE13-0015-02 for financial support. A.C-G. acknowledges the financial support from the European Research Council (ERC) under the European Union's Horizon 2020 research and innovation program (No.803004).

Supporting information

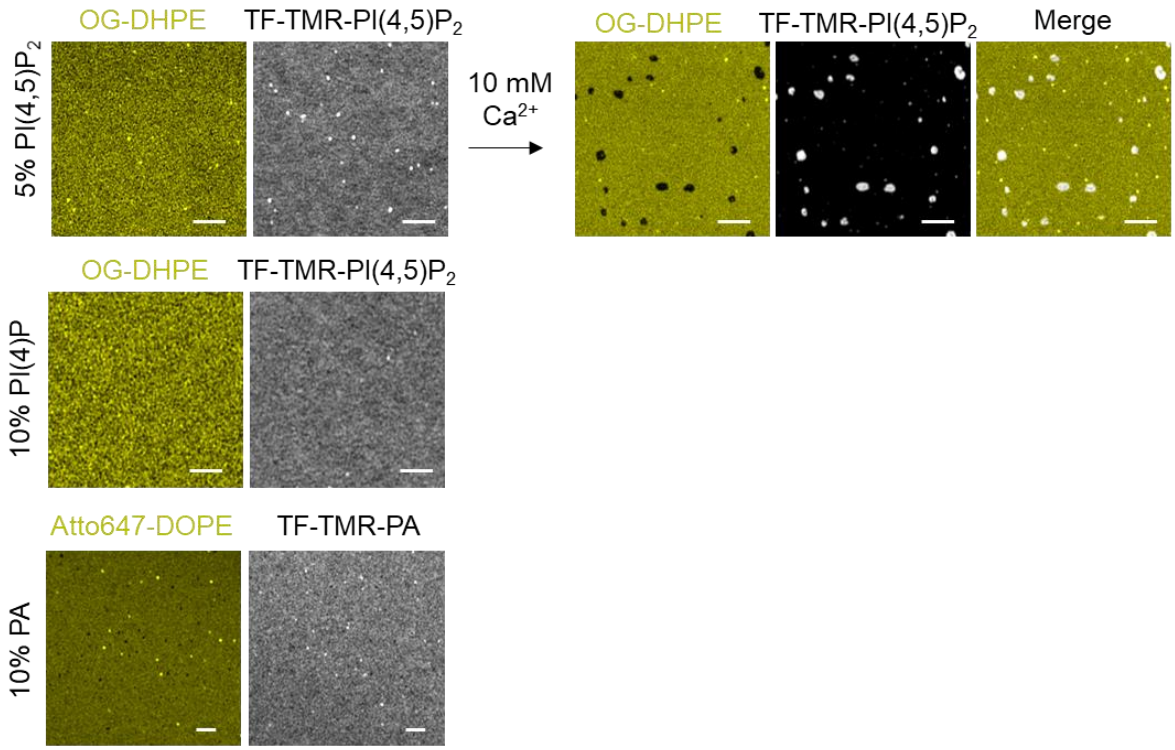

Figure 1- figure supplement 1. Representative airyscan images showing the lipid organization of different acidic TF-TMR lipid dyes ($PI(4,5)P_2$, PI(4)P and phosphatidic acid (PA) in gray) on lipid bilayers containing 20% mol of total negative charge relative to a neutral lipid dye (OG-DHPE or Atto647-DOPE). Lipid dyes were added to a final 0.2% mol at the expenses of the non-labeled counterpart. Addition of 10 mM of Ca^{2+} on lipid bilayers made of 5% $PI(4,5)P_2$ and doped with OG-DHPE and TF-TMR-$PI(4,5)P_2$ shows the detection of $PI(4,5)P_2$-enriched domains on this supported lipid bilayers. Scale bar, 2 µm.

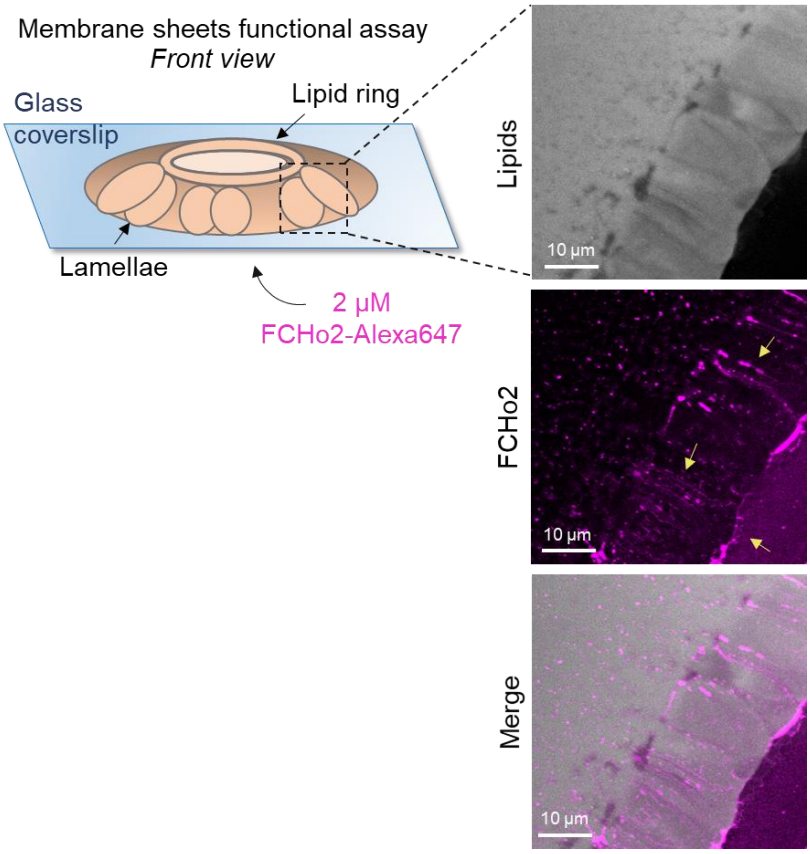

Figure 1- figure supplement 2. *Left*, schematic representation of the membrane sheets *in vitro* assay, as detailed by Itoh *et al*.(16), to test the functionality of recombinant full-length FCHo2-Alexa647. Membrane sheets were made using brain polar lipid extracts (Avanti). *Right*, representative still confocal images showing the formation of membrane tubes after addition of 2 µM of FCHo2, as indicated by yellow arrows.

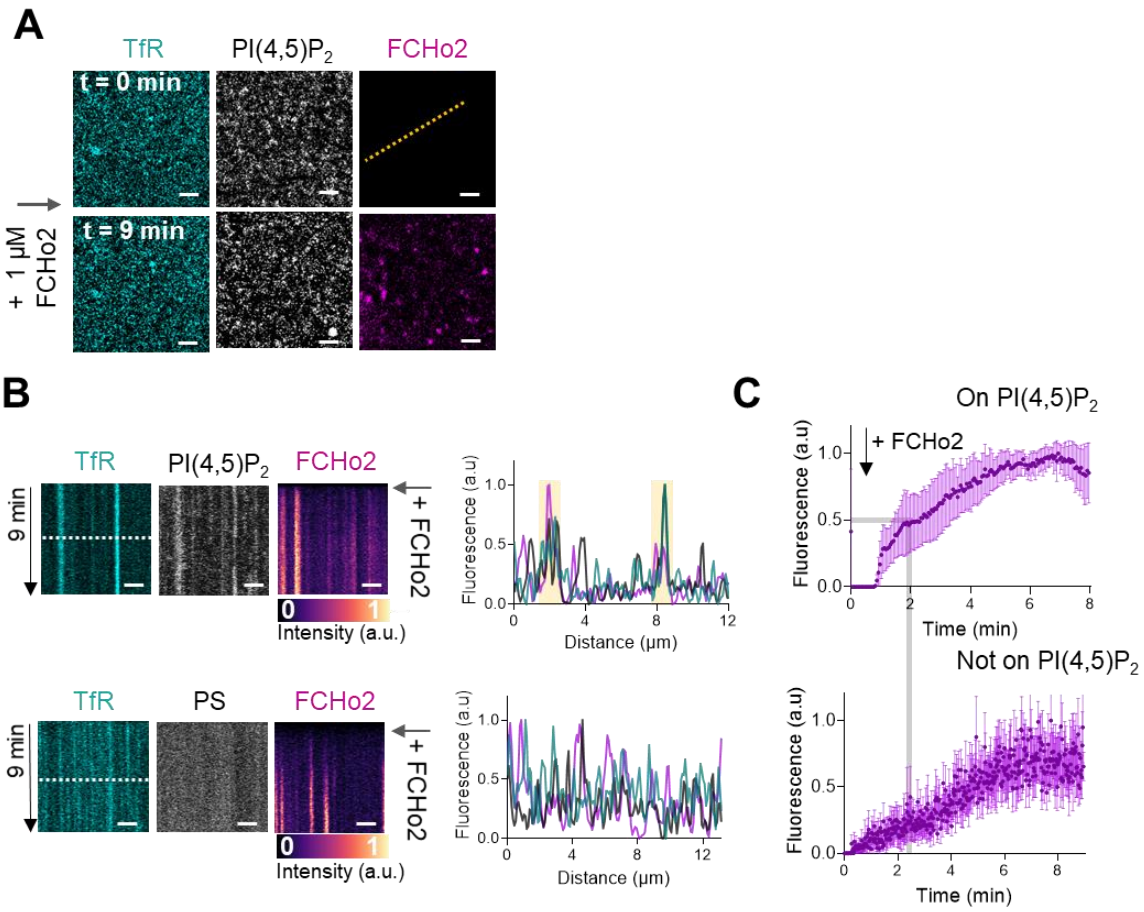

Figure 1- figure supplement 3. (A) Representative airyscan time-lapse showing the dynamics of $PI(4,5)P_2$ (gray), FCHo2 (magenta) and TfR-GFP (cyan) on plasma membrane sheets. Scale bar, 5 µm. (B) *Top*, kymograph analysis along the dashed line in A on plasma membrane sheets loaded with TF-TMR-$PI(4,5)P_2$ and intensity profile of the TfR (cyan), $PI(4,5)P_2$ (gray) and FCHo2 (magenta) along the dashed line in the kymograph. Time scale is 9 min. *Bottom*. Representative kymograph analysis on plasma membrane sheets loaded with TF-TMR-PS and intensity profile of the TfR (cyan), PS (gray) and FCHo2 (magenta) along the dashed line in the kymograph. Time scale is 9 min. Scale bar, 2 µm. (C) Fluorescence quantification over time of the FCHo2 recruitment (magenta) on $PI(4,5)P_2$-enriched regions (*top*) and not on $PI(4,5)P_2$ (bottom) on plasma membrane sheets. Each curve represents the mean ± s.d. of n = 7 recruitment kinetics from experimental replicates.

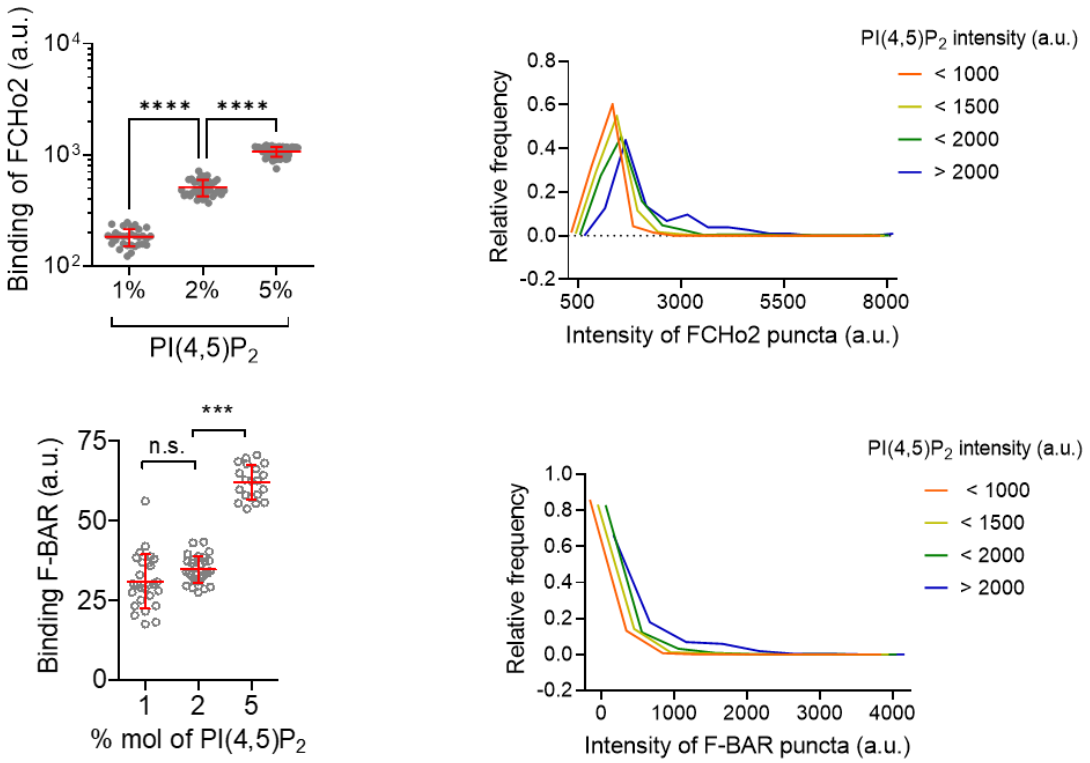

Figure 1- figure supplement 4. *Left*, binding of FCHo2 on lipid membranes containing different % mol of PI(4,5)P_2 (20% of total negative charge). Mean ± s.d. in red. one-way ANOVA (****, P < 0.0001). The number of regions of interest analyzed from experimental replicates was n=31, n=39, and n=54 for 1%, 2%, and 5% mol of PI(4,5)P_2, respectively. Binding of F-BAR on membranes containing different % mol of PI(4,5)P_2. Mean ± s.d. is displayed in red and one-way ANOVA (***, P = 0.0001). The number of regions of interest analyzed from experimental replicates was n=27, n=29, and n=20 for 1%, 2%, and 5% mol of PI(4,5)P_2 respectively. *Right*, relative frequency distribution of the intensity of FCHo2 and F-BAR puncta relative to the intensity of different PI(4,5)P_2 domains populations on 5% mol PI(4,5)P_2-membranes. The number of puncta analyzed from experimental replicates was n=11448 for FCHo2 and n=12828 for F-BAR. a.u., arbitrary units.

Figure 1- figure supplement 4 – source data 1. Binding and intensity of FCHo2 and F-BAR.

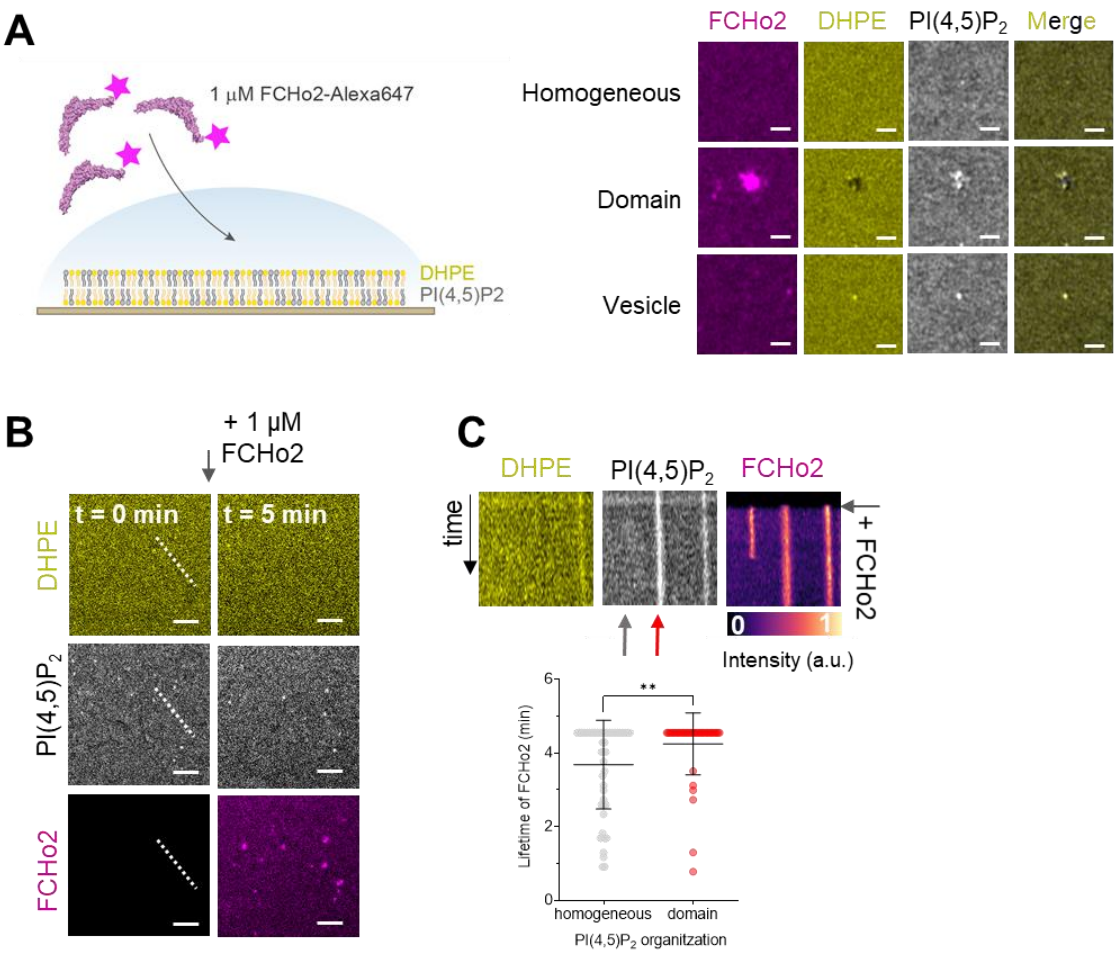

714

715 **Figure 1- figure supplement 5**. (A) *Left*, cartoon of the experimental setup to detect the interaction of FCHo2-A647 with
716 $PI(4,5)P_2$-enriched domains. *Right*, representative airyscan images showing the lipid organizations that were detected under
717 the experimental conditions: (i) an homogenous $PI(4,5)P_2$ organization, (ii) the formation of lipid domains and (iii) the
718 presence of adsorbed lipid vesicles. Scale bar, 1 µm. (B) Airyscan time-lapse showing the dynamics of FCHo2 (magenta) on
719 5% of $PI(4,5)P_2$ membranes doped with fluorescent $PI(4,5)P_2$ (gray) and DHPE (yellow). Scale bar, 2 µm. (C) *Top*,
720 kymograph analysis along the white dashed line in F. Time scale, 5 min. Scale, 2 µm. *Bottom*, lifetime of FCHo2 (in min)
721 relative to the $PI(4,5)P_2$ organization: homogeneous (grey) and on domains (red), as highlighted by the arrows in the
722 corresponding kymograph image. Mean ± s.d. in black. Welch's t-test (**, P = 0.0098). The number of FCHo2 puncta
723 analyzed from experimental replicates was n=50 and n=43 for a homogeneous and on domains, respectively.

724 **Figure 1- figure supplement 5 – source data 1.** Lifetime of FCHo2.

725

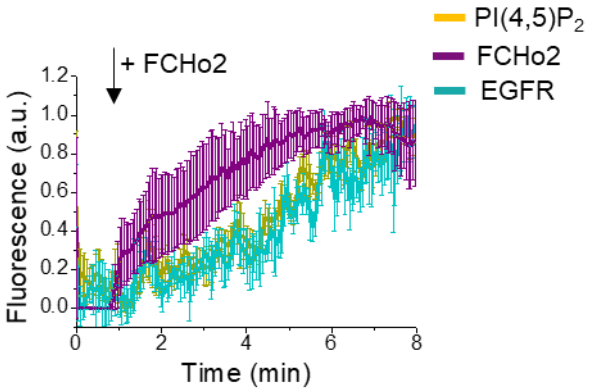

726

727 **Figure 1- figure supplement 6**. Fluorescence quantification over time of the EGFR (cyan), $PI(4,5)P_2$ (yellow) upon injection
728 of 1µM of FCHo2-Alexa647 (magenta) on EGFR-positive spots on plasma membrane sheets. Each curve represents the mean
729 ± s.d. of n = 9 recruitment kinetics from experimental replicates.

730

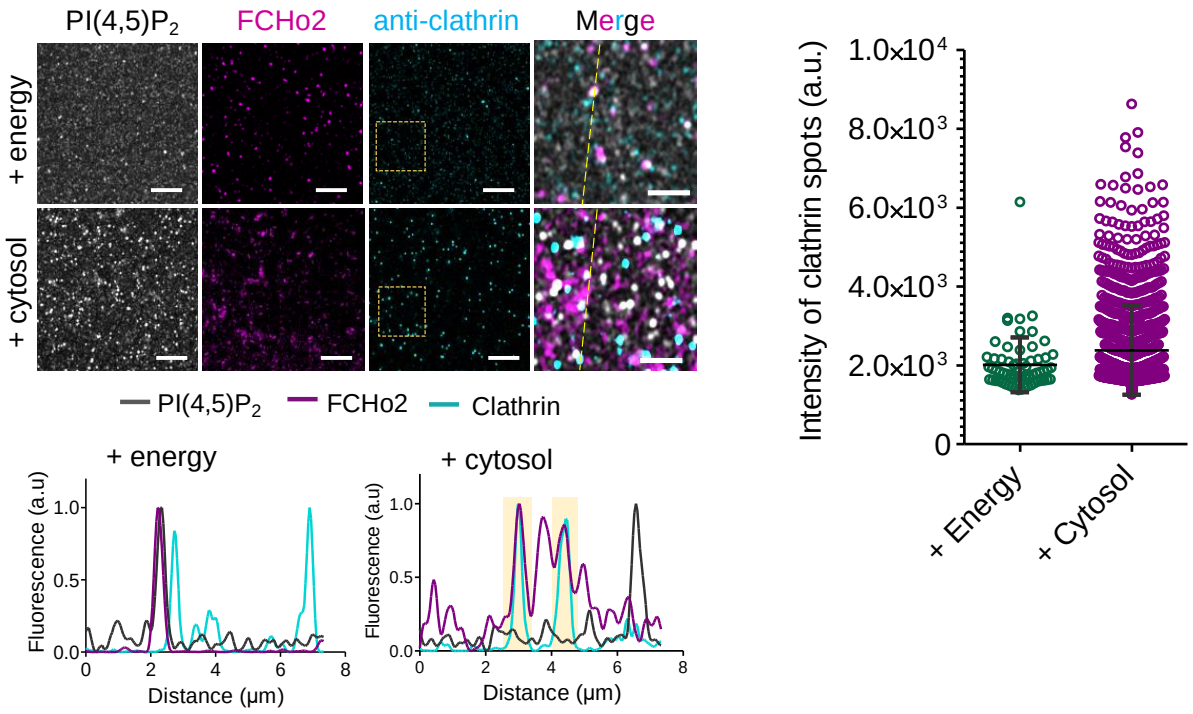

731

732 **Figure 2- figure supplement 1**. Representative airyscan images of the immunofluorescence assay showing the localization
733 of $PI(4,5)P_2$ (gray), FCHo2 (magenta) and clathrin (cyan, anti-clathrin antibody) on 5% $PI(4,5)P_2$-containing lipid bilayers
734 incubated with ATP and GTPγS (+ energy) or with the cytosolic extract and energy mix (+ cytosol). Scale bar, 5 µm.

735 **Figure 2- figure supplement 1 – source data 1.** Intensity of clathrin spots.

736

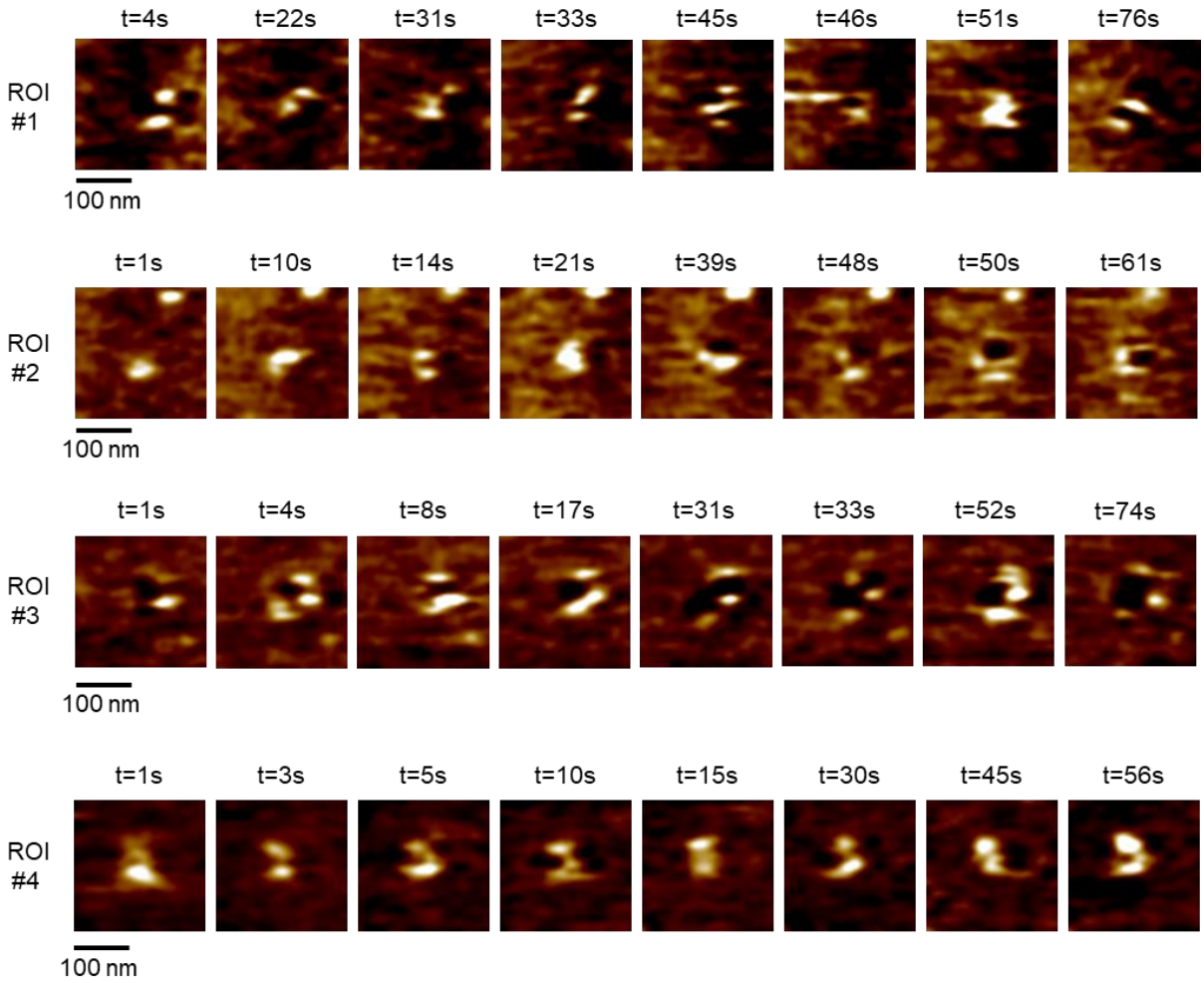

737

738

739 **Figure S8**. Representative HS-AFM frames of FCHo2 assembly on 5% PI(4,5)P_2-containing lipid bilayers. Different regions
740 of interest (ROI) show the FCHo2 ring formation stage, which took place within a time interval, Δt, of ~ 80 s.

741